

# SPH simulations of turbulent flow in curved pipes with different geometries. A comparison with experiments

**C. E. Alvarado-Rodríguez**

Dirección de Cátedras CONACYT, Av. Insurgentes Sur 1582,  
Crédito Constructor, Benito Juárez, 03940 Ciudad de México, Mexico  
and

Departamento de Ingeniería Química, DCNyE, Universidad de Guanajuato  
Noria Alta S/N, 36000 Guanajuato, Guanajuato, Mexico  
E-mail: carlos.alvarado@conacyt.mx

**L. Di G. Sigalotti\***

Departamento de Ciencias Básicas, Universidad Autónoma Metropolitana  
(UAM-A), Av. San Pablo 180, 02200 Ciudad de México, Mexico  
E-mail: leonardo.sigalotti@gmail.com

**J. Klapp, C. R. Fierro-Santillán, F. Aragón**

Instituto Nacional de Investigaciones Nucleares, (ININ)  
Carretera México-Toluca km. 36.5, La Marquesa, 52750 Ocoyoacac  
Estado de México, Mexico  
E-mail: jaime.klapp@inin.gob.mx, celia.fierro.estrellas@gmail.com, micme2003@yahoo.com.mx

**A. R. Uribe-Ramírez**

Departamento de Ingeniería Química, DCNyE, Universidad de Guanajuato  
Noria Alta S/N, 36000 Guanajuato, Guanajuato, Mexico  
E-mail: agustin@ugto.mx

## ABSTRACT

*The swirling secondary flow in curved pipes is studied in three-space dimensions using a weakly compressible Smoothed Particle Hydrodynamics (WCSPH) formulation coupled to new non-reflecting outflow boundary conditions. A large-eddy simulation (LES) model for turbulence is benchmarked with existing experimental data. After validation of the present model against experimental results for a 90° pipe bend, a detailed numerical study aimed at reproducing experimental flow measurements for a wide range of Reynolds numbers has been performed for different pipe geometries, including U pipe bends, S-shaped pipes and helically coiled pipes. In all*

---

\*Corresponding author.

*cases, the SPH calculated behavior shows reasonably good agreement with the measurements across and downstream the bend in terms of streamwise velocity profiles and cross-sectional contours. Maximum mean-root-square deviations from the experimentally obtained profiles are always less than  $\sim 1.8\%$ . This combined with the very good matching between the SPH and the experimental cross-sectional contours shows the uprising capabilities of the present scheme for handling engineering applications with streamline curvature, such as flows in bends and manifolds.*

**Keywords:** Computational fluid dynamics (CFD); Pipe flow; Pipe bends; Confined turbulent flow; Large-eddy simulation (LES); Mathematical modeling

## Nomenclature

Re Reynolds number

De Dean number

$\alpha$  Womersley number

$\rho$  Mass density,  $\text{kg m}^{-3}$ .

$\mathbf{v}$  Fluid velocity vector,  $\text{m s}^{-1}$ .

$\mathbf{g}$  Gravitational acceleration,  $\text{m s}^{-2}$ .

$p$  Pressure, Pa.

$\mathbf{F}$  Body force,  $\text{m s}^{-2}$ .

$c$  Sound speed,  $\text{m s}^{-1}$ .

$\mathbf{x}$  Position vector, m.

$\rho_0$  Reference density,  $\text{kg m}^{-3}$ .

$p_0$  Reference pressure, Pa.

$c_0$  Reference sound speed,  $\text{m s}^{-1}$ .

$\tilde{\mathbf{v}}$  Mean velocity,  $\text{m s}^{-1}$ .

$\mathbf{v}'$  Fluctuating velocity,  $\text{s}^{-1}$ .

$\bar{\rho}$  Reynolds-average density,  $\text{kg m}^{-3}$ .

$\bar{p}$  Reynolds-average pressure, Pa.

$T_{ij}$  SPS stress tensor,  $\text{kg m}^{-3} \text{s}^{-1}$ .

$\tilde{S}_{ij}$  Strain rate tensor,  $\text{s}^{-1}$ .

$\delta_{ij}$  Kronecker delta

- $t$  Time, s.
- $M$  Mach number
- $T$  Averaging time, s.
- $x, y, z$  Cartesian coordinates, m.
- $\nu$  Kinematic viscosity,  $\text{m}^2 \text{s}^{-1}$ .
- $\nu_t$  Smagorinsky eddy viscosity,  $\text{m}^2 \text{s}^{-1}$ .
- $\gamma$  Adiabatic exponent.
- $r$  Pipe radius, m.
- $d$  Pipe diameter, m.
- $R_c$  Bend mean radius of curvature, m.
- $L$  Pipe length, m.
- $P$  Coil pitch, m.
- $\dot{m}$  Mass flow rate,  $\text{kg s}^{-1}$ .
- $v_B$  Bulk flow velocity,  $\text{m s}^{-1}$ .
- $Q$  Volumetric flow rate,  $\text{m}^3 \text{h}^{-1}$ .
- $\omega$  Angular frequency,  $\text{s}^{-1}$ .
- $\Delta p$  Pressure drop, Pa.
- $f_c$  Fanning friction factor
- $\theta$  Angle
- $W$  Kernel function,  $\text{m}^{-3}$ .
- $h$  Smoothing length, mm.
- $m$  Particle mass, kg.
- $\Delta t$  Time step, s.
- $N$  Total number of particles.
- $n$  Number of neighboring particles.
- $a, b$  Particle indices.
- $\mathbf{v}_{wall}$  Fluid velocity at the pipe wall,  $\text{m s}^{-1}$ .
- 0 Reference index.

## **1 Introduction**

Flow in curved pipes and pipe bends are recurrent in many thermal engineering devices, such as oil and gas pipeline systems, water supply systems, automotive engines, fluid turbomachinery, power

generation plants and heat exchangers, just to mention a few. Such flows are complex in nature and often turbulent (i.e., inherently unsteady with strong secondary flows superimposed to the streamwise flow). Therefore, in response to the always increasing practical interest to understand the physical mechanisms underlying turbulent flows through pipe bends and elbows, numerous experimental and numerical investigations have been devoted to their study in curved pipes and ducts of various cross-sectional shapes. In contrast to straight pipe flow, pressure drop and heat/mass transfer are both enhanced in pipe bends, whereas turbulent flow motion can cause vibrations and mechanical fatigue of the pipeline system, eventually leading to failure.

Representative experimental measurements of turbulent flow in curved pipes have been conducted by Humphrey et al. [1], Taylor et al. [2], Enayet et al. [3], Chang et al. [4], Sreenivasan and Strykowski [5], Azzola et al. [6], Fiedler [7], Sudo et al. [8, 9, 10], El-Gammal et al. [11], Hellström et al. [12], De Amicis et al. [13], Mazhar et al. [14] and Oki et al. [15] to mention a few. In particular, the turbulent flow downstream a 90° pipe bend have been investigated by Humphrey et al. [1], Taylor et al. [2], Enayet et al. [3], Sudo et al. [8, 10], and more recently by Kalpakli and Örlü [16], Mazhar et al. [14] and Kalpakli et al. [17]. In general, most of these studies report profiles of the longitudinal and circumferential velocity components as well as cross-stream velocity contours both upstream the bend inlet, inside the bend and downstream the bend outlet for a range of Reynolds (Re) numbers. On the other hand, measurements of turbulent flow through circular- and rectangular-sectioned U-bends have also been reported by Chang et al. [4], Azzola et al. [6] and Sudo et al. [9]. Moreover, experimental works in helically coiled pipes were focused mainly on measuring pressure or temperature data and deducing characteristics of the flow. In particular, Sreenivasan and Strykowski [5] studied the stabilization effects of the flow in the coiled section, and more recently Cioncolini and Santini [18] and Hayamizu et al. [19] studied the curvature and torsion effects on the flow regarding the laminar to turbulent transition. On the other hand, experiments by Gupta et al. [20], Pimenta and Campos [21] and De Amicis et al. [13] were addressed to measure the pressure drop for helical pipes under laminar flow conditions. Pulsatile flow in S-shaped pipes was investigated by Oki et al. [15] using conditions for the flow field resembling an automotive engine environment.

As a fluid flows through a pipe bend or elbow, a secondary flow arises due to the cross-sectional pressure gradient that takes place in the radial direction of the bend curvature as a result of the centrifugal force acting on the fluid [8]. The strength of the secondary flow depends on the radius of the bend curvature,  $R_c$ , and the Reynolds number, defined as  $Re = u_B d / \nu$ , where  $u_B$  is the bulk velocity,  $d$  is the pipe diameter and  $\nu$  is the kinematic viscosity. If the ratio  $R_c/d < 1.5$ , flow separation occurs

immediately downstream the bend inlet, giving rise to increased pressure losses [12]. Conversely, if  $R_c/d > 1.5$ , a secondary flow consisting of two counter-rotating vortices forms, the so-called Dean vortices [22]. Under these conditions, the streamwise velocity contours become C-shaped and the velocity profiles distort as they are shifted away from the center of curvature of the bend [12].

Due to its complex and resource-demanding character, numerical simulations of flow in curved pipes have only started to appear in the last two decades in parallel with the advent of increasing computing facilities. In-depth Computational Fluid Dynamics (CFD) studies of water flow in a 90° elbow of circular cross-section with  $R_c/d = 1.4$  and  $Re = 5.4 \times 10^5$  were first reported by Homicz [23] with the aid of the software FLUENT, where finite volume methods (FVM) were employed to solve the Reynolds-Averaged Navier-Stokes (RANS) equations coupled to a  $k-\epsilon$  closure for the turbulence model. Further FVM calculations of water flow in pipe bends were presented by Tanaka et al. [24] for various values of  $Re$  and  $R_c/d$ , using the Large Eddy Simulation (LES) model for turbulence. A database for LES and Direct Numerical Simulations (DNS) on pipe bend flows can be found in Refs. [25,26]. More recently, Kim et al. [27] performed numerical simulations of Sudo et al.'s [8] experiments using the FVM-based OpenFOAM software along with a comparative analysis to choose the turbulence model that better reproduced the experimental data. They found that the Renormalization Group (RNG)  $k-\epsilon$  model gave better results for primary streamwise and secondary swirling velocity profiles than the other turbulence models for  $R_c/d > 1.5$  and  $Re$  ranging from  $5 \times 10^4$  to  $2 \times 10^5$ . The OpenFOAM solver was also employed by Röhrig et al. [28] for simulations of turbulent flow in a 90° pipe bend. They performed a comparative computational assessment between the wall-resolved LES and various RANS models for  $Re$  varying from  $1.4 \times 10^3$  to  $3.4 \times 10^3$ . By comparing their results with the experimental data of Kalpakli and Örlü [16], they assessed the superiority of LES over the applied RANS methods, however at the cost of much greater computational effort. In particular, they found that LES reproduced the experimental profiles for the streamwise mean velocity and turbulent intensity just behind the elbow much better than RANS, while inside the bend both approaches yielded comparatively similar mean velocity profiles and pressure coefficients. Further FVM-based calculations of turbulent flow in 90° elbows were presented by Dutta et al. [29] and Wang et al. [30].

On the other hand, the effect of the helical geometry on the flow field was also investigated numerically by a number of authors. In particular, Di Piazza and Ciofalo [31] assessed the applicability of the classical  $k-\epsilon$  and  $k-\omega$  closure models to the prediction of pressure drop and heat transfer in coiled tubes, using the numerical code ANSYS CFX 11 for a broad range of  $Re$ , Prandtl numbers ( $Pr$ ) and coil curvatures, while Jayakumar et al. [32] studied the flow characteristics in helical pipes with various derived

correlations for the prediction of local values of the Nusselt number ( $Nu$ ) as a function of the average  $Nu$  and the angular position along the pipe circumference. Later on, De Amicis et al. [13] investigated the laminar flow in helically coiled pipes with the aid of three commercial CFD softwares, namely the FLUENT, the OpenFOAM and the Finite Element based COMSOL Multiphysics packages. All these simulations predicted a centrifugal force acting on the fluid as a consequence of the duct curvature and a cross-sectional pressure gradient, which led to the formation of two counter-rotating vortices that are symmetrical in the case of a toroidal pipe. More recently, Tang et al. [33] carried out CFD simulations to explore the variations in the velocity distribution, pressure field and secondary flow when varying the curvature radius, the coil pitch and the Dean number, defined as  $De = Re(r/R_c)^{1/2}$ , where  $r$  is the pipe radius. Moreover, numerical simulations of oscillatory flow in curved pipes are of interest in the biomedical sciences. For example, Glenn et al. [34] analyzed pulsatile flow in a curved artery model, while van Wyk et al. [35] performed simulations of the pulsatile blood flow in a  $180^\circ$  curved artery. An account of the state-of-the-art research concerning turbulent flow in curved pipes, covering experimental and numerical work, can be found in the review paper by Kalpakli Vester et al. [36].

Numerical simulations of Poiseuille flow at low and moderate Reynolds numbers in straight channels and pipes using Smoothed Particle Hydrodynamics (SPH) have been performed by a number of authors [37, 38, 39, 40, 41, 42]. In particular, simulations of open-channel flows have been primarily addressed to test the implementation of inlet, outlet and wall boundary conditions in SPH [43, 44, 45]. In comparison, SPH simulations of curved pipe flows are correspondingly scarcer. Among the few examples found in the literature are the works of Hou et al. [46], who employed SPH methods to study flow separation in two-dimensional, right-angled bends for different ratios of the channel widths and different turning angles, and Alvarado-Rodríguez et al. [47], who performed three-dimensional SPH calculations of Sudo et al.'s [10] experiment for flow in a square-sectioned  $90^\circ$  pipe bend and provided a direct comparison with Rup et al.'s [48] FLUENT-based simulations of the same experiment. SPH models of supercritical flow in circular conduit bends have also started to appear [49]. In this work we focus on three-dimensional (3D), LES models of single-phase flow in curved pipes with the use of a weakly compressible SPH (WCSPH) scheme [50] coupled with a new formulation for modeling non-reflecting outlet boundary conditions. The goal is to test the new outflow boundary conditions and show the upris- ing capabilities of the present scheme for handling engineering applications with streamline curvature, such as flows in bends and manifolds, and reproducing experimental results with very good accuracy. Flow in curved pipes is studied for different pipe geometries, including  $90^\circ$  and U pipe bends, S-shaped pipes and helically coiled pipes. The numerical simulations are addressed to describe the effects of

geometry on the flow through the onset of secondary flow, the deformation of the axial velocity profile and reproduce the results of existing calibrated experiments.

The governing equations, the SPH methodology and the implementation of the boundary conditions are described in Section 2. The validation of the numerical scheme is given in Section 3. Section 4 describes the numerical results and provides direct comparison with experimental and numerical data in the literature. In all cases, the results obtained from the SPH simulations are found to be in good agreement with the experimental measurements. Finally, Section 5 contains the main conclusions.

## 2 Numerical methods and models

### 2.1 Governing equations

The basic equations describing the flow of a fluid in a curved pipe are given by the Navier-Stokes equations

$$\frac{d\rho}{dt} = -\rho \nabla \cdot \mathbf{v}, \quad (1)$$

$$\frac{d\mathbf{v}}{dt} = -\frac{1}{\rho} \nabla p + \nu \nabla^2 \mathbf{v} + \mathbf{g}, \quad (2)$$

where  $\rho$  is the mass density,  $\mathbf{v}$  is the fluid velocity vector,  $p$  is the pressure,  $\nu$  is the coefficient of kinematic viscosity,  $\mathbf{g}$  is the acceleration due to gravity and  $d/dt = \partial/\partial t + \mathbf{v} \cdot \nabla$  is the material time derivative. Equations (1) and (2) express the mass and momentum conservation laws, respectively. The dynamical pressure is related to the density by means of the Murnaghan-Tait equation [50]

$$p = p_0 \left[ \left( \frac{\rho}{\rho_0} \right)^\gamma - 1 \right], \quad (3)$$

where  $\gamma = 7$ ,  $p_0 = c_0^2 \rho_0 / \gamma$ ,  $\rho_0$  is a reference density and  $c_0$  is the sound speed at the reference density. The term  $p_0$  governs the relative density fluctuations  $|\rho - \rho_0|/\rho_0 \sim M^2$ , where  $M$  is the Mach number. Typically  $M^2$  is set to 0.01 in order to enforce density fluctuations within 1%. This is achieved by artificially setting the reference sound speed to be at least 10 times higher than the maximum expected fluid velocity [50]. This ensures that the compressibility effects are purely acoustic so that they can be considered to be superimposed to the main flow with almost no interaction. Therefore, a Mach number equal to 0.1 satisfactorily enforces the fluid incompressibility condition. A very robust WCSPH scheme,

known in the literature as  $\delta$ -SPH, was introduced by Antuono et al. [51], which stabilizes the conventional WCSPH scheme against noisy and oscillatory pressure fields. However, preliminary test calculations with this variant and the standard WCSPH formulation implemented here showed no differences in the final results for turbulent flow in a 90° pipe elbow.

Equations (1) and (2) are replaced by spatially-filtered equations pertinent to the LES method. This will allow resolving the larger turbulent scales while still modeling in an approximate manner the smaller ones. In particular, in the SPH framework coherent turbulent structures in the fluid can be followed by implementing a sub-particle scaling (SPS) technique [52]. This is achieved by dividing the flow velocity into its mean (or ensemble average) part and the fluctuations around it as  $\mathbf{v} = \tilde{\mathbf{v}} + \mathbf{v}'$ , where the mean  $\tilde{\mathbf{v}}$  is given by the density-weighted Favre-filtering

$$\tilde{\mathbf{v}} = \frac{1}{\bar{\rho}} \frac{1}{T} \int_t^{t+T} \rho(\mathbf{x}, t) \mathbf{v}(\mathbf{x}, t) dt, \quad (4)$$

where  $T$  is an averaging time and  $\bar{\rho}$  is the mean density given by the conventional Reynolds-averaged density. Applying the Favre filtering to Eqs. (1) and (2) yields the spatially filtered Navier-Stokes equations

$$\frac{d\bar{\rho}}{dt} = -\bar{\rho} \nabla \cdot \tilde{\mathbf{v}}, \quad (5)$$

$$\frac{d\tilde{\mathbf{v}}}{dt} = -\frac{1}{\bar{\rho}} \nabla \bar{p} + \frac{\mathbf{v}}{\bar{\rho}} [\nabla \cdot (\bar{\rho} \nabla)] \tilde{\mathbf{v}} + \frac{\mathbf{v}}{\bar{\rho}} \nabla \cdot \mathbf{T} + \mathbf{g}, \quad (6)$$

where  $\mathbf{T}$  is the SPS stress tensor, which in component form can be written as

$$T_{ij} = \bar{\rho} v_t \left( 2\tilde{S}_{ij} - \frac{2}{3}\tilde{S}_{kk}\delta_{ij} \right) - \frac{2}{3}\bar{\rho} C_I \Delta^2 \delta_{ij} |\tilde{S}|^2. \quad (7)$$

Here  $\tilde{S}_{ij}$  is the Favre-filtered strain rate tensor given by

$$\tilde{S}_{ij} = \frac{1}{2} \left( \frac{\partial \tilde{v}_i}{\partial x_j} + \frac{\partial \tilde{v}_j}{\partial x_i} \right), \quad (8)$$



$C_I = 0.00066$ ,  $\nu_t = (C_s \Delta)^2 |\tilde{S}|$ , with  $C_s = 0.12$ , is the Smagorinsky eddy viscosity,  $|\tilde{S}| = (2\tilde{S}_{ij}\tilde{S}_{ij})^{1/2}$  is the local strain rate,  $\delta_{ij}$  is the Kronecker delta and  $\Delta$  is a measure of the finite particle size. For practical purposes,  $\Delta$  is set equal to the local particle smoothing length  $h$  (see below).

## 2.2 SPH solver

Equations (5) and (6) are solved numerically using a variant of DualSPHysics [53], an open-source CFD toolbox, which is based on the SPH methodology [54, 55]. The SPH method is a fully Lagrangian, mesh-free scheme for complex fluid-flow simulations, where the fluid is represented by a finite number of discrete particles that characterize the flow attributes. Due to its Lagrangian character, SPH tracks material history information of the system on the moving particles which carry all field information such as position, density and velocity.

SPH consists of two steps. One is the kernel approximation in which the estimate of a function,  $f(\mathbf{x})$ , is given by the volume integral

$$\langle f(\mathbf{x}) \rangle = \int_{\Omega} f(\mathbf{x}') W(|\mathbf{x} - \mathbf{x}'|, h) d\mathbf{x}', \quad (9)$$

$\forall \mathbf{x} \in \Omega$ , where  $\Omega \subset \mathbf{R}^3$  is the spatial domain of integration,  $W$  is the kernel (or interpolation) function, which is assumed to be spherically symmetric in its support domain  $\Gamma$  ( $\Gamma \subset \Omega$  with boundary  $\partial\Gamma$ ) and  $h$  is the so-called smoothing length, which is a dilation parameter that determines the (compact) support size of the kernel. If the spatial domain  $\Omega$  is divided into  $N$  sub-domains, labeled  $\Omega_a$ , each of which encloses a particle  $a$  at position  $\mathbf{x}_a \in \Omega_a$ , the discrete equivalent of Eq. (9) becomes

$$f_a = \sum_{b=1}^n f_b W_{ab} \Delta V_b, \quad (10)$$

where  $f_a = \langle f(\mathbf{x}_a) \rangle$ ,  $W_{ab} = W(|\mathbf{x}_a - \mathbf{x}_b|, h)$ ,  $\Delta V_b$  is the volume of particle sub-domain  $\Omega_b$  and the summation is taken over the  $n$  neighbors of particle  $a$  within the support  $\Gamma$  of the kernel. A schematic drawing of the kernel in two dimensions is shown in Fig. 1. A field variable at particle  $a$  is approximated using the corresponding field variable of all neighboring particles  $b$  within the support domain of radius  $kh$ , where  $k$  is a scale parameter usually  $\leq 2$  for most kernel functions. The support of the kernel shown in Fig. 1 as a circle is actually a sphere of radius  $kh$  in three dimensions. Because of its compact nature, at

radial distances from particle  $a$  greater than  $kh$  the kernel vanishes so that the number of neighbors  $n$  is always a small subset of the total number of particles. The neighbors of particle  $a$  can be unevenly distributed within the support of the kernel and their instantaneous positions  $\mathbf{x}_b = (x_b, y_b, z_b)$  are here defined with respect to an inertial frame at rest with the pipe walls. Under the assumption of a mass density distribution  $\rho(\mathbf{x})$ , the particle mass,  $m_b$ , is defined as  $\rho_b \Delta V_b$  so that Eq. (10) is finally rewritten as

$$f_a = \sum_{b=1}^n \frac{m_b}{\rho_b} f_b W_{ab}. \quad (11)$$

This step is called particle (or SPH) approximation. Density fluctuations are calculated using the continuity equation (5), which in SPH form can be written as

$$\frac{d\rho_a}{dt} = \sum_{b=1}^n m_b (\mathbf{v}_a - \mathbf{v}_b) \cdot \nabla_a W_{ab}, \quad (12)$$

where the density may be either the local density  $\rho$  or the particle-scale density  $\bar{\rho}$  depending on whether we are dealing with laminar or turbulent flows. The same applies to the velocity field where  $\mathbf{v}$  may represent a local velocity (for laminar flows) or the Favre-filtered velocity  $\tilde{\mathbf{v}}$  (for turbulent flows).

The source terms in Eqs. (2) and (6) are written in SPH form using the symmetric representation proposed by Colagrossi and Landrini [56] for the pressure gradient and the representations given by Lo and Shao [57] for the laminar viscous term and the SPS stresses. Therefore, in SPH form Eq. (6) becomes

$$\begin{aligned} \frac{d\mathbf{v}_a}{dt} = & - \frac{1}{\rho_a} \sum_{b=1}^n \frac{m_b}{\rho_b} (p_a + p_b) \nabla_a W_{ab} \\ & + 4\mathbf{v} \sum_{b=1}^n m_b \frac{\mathbf{v}_a - \mathbf{v}_b}{\rho_a + \rho_b} \frac{\mathbf{x}_{ab} \cdot \nabla_a W_{ab}}{|\mathbf{x}_{ab}|^2 + \epsilon^2} \\ & + \sum_{b=1}^n m_b \left( \frac{\mathbf{T}_a}{\rho_a^2} + \frac{\mathbf{T}_b}{\rho_b^2} \right) \cdot \nabla_a W_{ab} + \mathbf{g}, \end{aligned} \quad (13)$$

where  $\mathbf{x}_{ab} = \mathbf{x}_a - \mathbf{x}_b$  and  $\epsilon^2 = 0.01h^2$ . The tilde operator over the velocity and the bars over the density and pressure have been dropped for simplicity. In Eqs. (12) and (13) the kernel function  $W_{ab}$  is evaluated

using the symmetrization [58]

$$W_{ab} = \frac{1}{2} [W(|\mathbf{x}_a - \mathbf{x}_b|, h_a) + W(|\mathbf{x}_a - \mathbf{x}_b|, h_b)], \quad (14)$$

whenever  $h_a \neq h_b$ . Note that the SPH representation of Eq. (2) for laminar flows can be recovered from Eq. (13) by simply dropping the SPS stress term. Particle positions are determined by solving simultaneously the equation

$$\frac{d\mathbf{x}_a}{dt} = \mathbf{v}_a + \frac{\beta x_0 v_{\max}}{M} \sum_{b=1}^N m_b \frac{\mathbf{x}_{ab}}{(\mathbf{x}_{ab} \cdot \mathbf{x}_{ab})^{3/2}}, \quad (15)$$

where the second term on the right-hand side is added to prevent the growth of SPH discretization errors due to anisotropies in the distribution of particle positions [59]. Here  $\beta = 0.04$ ,  $v_{\max}$  is the maximum fluid velocity,  $M$  is the total mass of the system and

$$x_0 = \frac{1}{N} \sum_{b=1}^N (\mathbf{x}_{ab} \cdot \mathbf{x}_{ab})^{1/2}, \quad (16)$$

is the mean distance between particle  $a$  and all other particles. The summations in Eqs. (15) and (16) are over the total number of particles filling the computational fluid domain.

A Wendland  $C^2$  function is adopted as the interpolation kernel [60, 61]

$$W(q, h) = \frac{21}{2\pi h^3} (1 - q)^4 (1 + 4q), \quad (17)$$

for  $q \leq 1$  and zero otherwise, where  $q = |\mathbf{x} - \mathbf{x}'|/h$ . These interpolating functions are known to improve the convergence properties of SPH and suppress the pairing instability regardless of the number of neighbors within the kernel support [61]. Particle velocities and positions are updated using a temporally second-order accurate Verlet scheme for time integration of Eqs. (13) and (15), given by the following

difference formulae

$$\begin{aligned}\rho_a^{n+1} &= \rho_a^{n-1} + 2\Delta t \left( \frac{d\rho_a}{dt} \right)^n, \\ \mathbf{v}_a^{n+1} &= \mathbf{v}_a^{n-1} + 2\Delta t \left( \frac{d\mathbf{v}_a}{dt} \right)^n, \\ \mathbf{x}_a^{n+1} &= \mathbf{x}_a^n + \Delta t \mathbf{v}_a^n + 0.5\Delta t^2 \left( \frac{d\mathbf{v}_a}{dt} \right)^n,\end{aligned}\tag{18}$$

where  $\Delta t = t^{n+1} - t^n$ . In order to prevent the time integration to yield results that may diverge from the actual solution and improve the numerical coupling between Eqs. (13) and (15) during the evolution, the above scheme is replaced every 40 timesteps by the alternative scheme

$$\begin{aligned}\rho_a^{n+1} &= \rho_a^n + \Delta t \left( \frac{d\rho_a}{dt} \right)^n, \\ \mathbf{v}_a^{n+1} &= \mathbf{v}_a^n + \Delta t \left( \frac{d\mathbf{v}_a}{dt} \right)^n, \\ \mathbf{x}_a^{n+1} &= \mathbf{x}_a^n + \Delta t \mathbf{v}_a^n + 0.5\Delta t^2 \left( \frac{d\mathbf{v}_a}{dt} \right)^n.\end{aligned}\tag{19}$$

The optimal timestep calculation is guided by the following prescriptions

$$\begin{aligned}\Delta t_f &= \min_a (h|dv_a/dt|^{-1})^{1/2}, \\ \Delta t_{v,a} &= \max_b |h\mathbf{x}_{ab} \cdot \mathbf{v}_{ab} / (\mathbf{x}_{ab} \cdot \mathbf{x}_{ab} + \epsilon^2)|, \\ \Delta t_{cv} &= \min_a [h(c_a + \Delta t_{v,a})^{-1}], \\ \Delta t &= 0.3 \min(\Delta t_f, \Delta t_{cv}),\end{aligned}\tag{20}$$

where the maximum and minima are taken over all particles in the system,  $v_a = (\mathbf{v}_{ab} \cdot \mathbf{v}_{ab})^{1/2}$  and  $c_a$  is the sound speed for particle  $a$ .

### 2.3 Boundary conditions

No-slip boundary conditions are implemented at the pipe walls using the method of dynamic boundary particles developed by Crespo et al. [62, 63]. To do so, the pipe surface is covered by a layer of

uniformly-spaced external particles, which are used to cope with the problem of kernel deficiency outside the computational domain. A layer of particles is also employed to represent the solid wall, which are updated using the same loop as the inner fluid particles and so they are forced to satisfy Eqs. (13) and (15). However, they are not allowed to move accordingly so that their initial positions and velocities ( $\mathbf{v}_{\text{wall}} = \mathbf{0}$ ) remain unchanged in time. In this way, the presence of the wall is modeled by means of a repulsive force, which is derived from the source of the momentum Eq. (13) and includes the effects of compressional, viscous and gravitational forces. This force is exerted by the wall particles on the fluid particles only when the latter get closer than a distance  $d_a = 2h$  from the wall. Across the wall, an external particle, say  $a'$ , is assigned a mass  $m_{a'} = m_{\text{wall}}$  and a density  $\rho_{a'} = \rho_{\text{wall}}$ , while Neumann boundary conditions for the pressure are ensured by setting  $p_{a'} = p_{\text{wall}}$ .

An inflow zone upstream the pipe inlet is used to set proper inlet boundary conditions. In this zone, a steady inlet velocity without temporal fluctuations is assumed, which may correspond to either a flat profile or a fully developed Hagen-Poiseuille flow. The assumption of steady flow conditions at the inlet is justified because disturbances there are expected to be low due to the long straight pipe segment upstream the bend for most models. For the purposes of comparing the numerical results with calibrated experiments in the literature, the boundary conditions employed in the simulations are set identically with the corresponding experimental cases. On the other hand, outflow boundary conditions are designed in such a way that the flow is allowed to cross the pipe outlet without being significantly reflected back [47]. To this end an outflow zone is defined downstream the pipe exit plane. In all simulations the lengths of the inflow and outflow zones are chosen to be the same and equal to 5 initial uniform particle separations in the streamwise direction. The method then allows for anisotropic wave propagation across the outlet, where the velocity vector of particles incident on the outlet and entering the outflow zone obeys the outgoing wave equation [47]

$$\frac{\partial \mathbf{v}}{\partial t} + v_x \frac{\partial \mathbf{v}}{\partial x} - \mathbf{v} \left( \frac{\partial^2 \mathbf{v}}{\partial y^2} + \frac{\partial^2 \mathbf{v}}{\partial z^2} \right) = \mathbf{0}, \quad (21)$$

where  $\mathbf{v} = (v_x, v_y, v_z)$ . This equation is valid for the case where the streamwise flow is assumed to be along the  $x$ -direction. The velocity of particles in the outflow zone is evolved using Eq. (21). For an

outflow particle, say  $o$ , this equation can be written in SPH form as

$$\begin{aligned} \frac{\partial \mathbf{v}_o}{\partial t} = & -v_{x,o} \sum_{b=1}^n \frac{m_b}{\bar{\rho}_{ob}} (\mathbf{v}_b - \mathbf{v}_o) \frac{\partial W_{ob}}{\partial x_o} \\ & + 2v \sum_{b=1}^n \frac{m_b}{\rho_b} \frac{(\mathbf{v}_b - \mathbf{v}_o)}{|\mathbf{x}_{ob}|^2 + \epsilon^2} \left( y_{ob} \frac{\partial W_{ob}}{\partial y_o} + z_{ob} \frac{\partial W_{ob}}{\partial z_o} \right), \end{aligned}$$

where  $\mathbf{x}_{ob} = \mathbf{x}_o - \mathbf{x}_b$ ,  $y_{ob} = y_o - y_b$ ,  $z_{ob} = z_o - z_b$  and  $\bar{\rho}_{ob} = (\rho_o + \rho_b)/2$ . Since in most problems of interest the inlet and outlet mass rates and cross-sectional areas may differ, a particle leaving the outflow zone is temporarily stored in a reservoir buffer and its velocity is automatically zeroed. Only when an inflow particle crosses the pipe inlet, a particle is removed from the buffer and placed in the upstream side of the inflow zone with the desired prescribed density and velocity values. The initial number of reservoir particles is arbitrarily set and can be as large as needed. According to the usual SPH procedures, outflow particles near the outlet may have some fluid particles as neighbors, thereby allowing fluid information to be propagated into the outflow zone. The numerical stability of Eq. (22) is improved when the streamwise velocity component,  $v_{x,o}$ , is smoothed according to

$$v_{x,o} = \sum_{b=1}^n \frac{m_b}{\rho_b} v_{x,b} W_{ob}, \quad (22)$$

where particle  $o$  can have neighbors of both types (i.e., fluid and outflow particles) depending on how close it is from the pipe outlet. The position of outflow particles is determined by solving the equation

$$\frac{d\mathbf{x}_o}{dt} = \mathbf{v}_o, \quad (23)$$

which, together with Eq. (22), is integrated using the Verlet scheme described by Eqs. (18) and (19).

### 3 Convergence test and numerical validation

In order to provide internally coherent flow conditions for the subsequent simulations of bent pipes, a convergence test was carried out by varying the total number of particles,  $N$ . The same test was also employed to validate the numerical procedure, which consists of simulating Enayet et al.'s [3] experiments of water flow in a 90° bend of circular cross-section at various bulk Reynolds numbers.

The geometry and dimensions of the test bend are shown in Fig. 2. The pipe diameter is  $d = 48$  mm and the radius of curvature is  $R_c = 2.8d = 134.4$  mm. As shown in Fig. 2, a horizontal straight pipe 240 mm long and of the same diameter is fitted upstream to the bend and a second straight pipe 480 mm long is fitted downstream. The bulk flow velocity is defined as

$$v_B = \frac{4\dot{m}}{\pi\rho d^2}, \quad (24)$$

where  $\rho$  is the density of water and  $\dot{m}$  is the mass flow rate given by  $\dot{m} = \pi\rho v d Re/4$ , and  $\nu$  is the kinematic viscosity of water (taken to be  $\approx 10^{-6} \text{ m}^2 \text{ s}^{-1}$  at  $20^\circ\text{C}$ ) and  $Re$  is the diameter-based bulk Reynolds number. The coordinate axes are chosen such that the streamwise local mean velocity is always along the  $x$ -direction ( $\tilde{v} = v_x$ ). Experimental results for this test case were obtained by Enayet et al. [3] for laminar flow at  $Re = 500$  and  $1093$  and for turbulent flow at the maximum obtainable  $Re = 43000$ , corresponding to values of  $v_x = 10.5 \text{ mm s}^{-1}$ ,  $23 \text{ mm s}^{-1}$  and  $0.92 \text{ m s}^{-1}$ , respectively.

The results of the convergence study are reported in Fig. 3, where the streamwise velocity profiles in the horizontal ( $y$ ) and vertical ( $z$ ) directions normalized to  $v_B$  are shown for the various  $Re$  and resolutions considered. The profiles for  $Re = 500$ ,  $1093$  and  $43000$  are compared with the experimental data of Enayet et al. [3] at  $212.16$  mm from the pipe inlet (upstream the bend inlet). Table 1 lists the deviations between the experimental and numerical profiles in terms of the root-mean-square error (RMSE). The numerical profiles in Fig. 3 show an asymptotic tendency to globally converge as the number of particles is increased from  $N = 247790$  to  $4038085$ . This is also seen in Table 1, where the RMSE values decrease progressively with the number of particles. Independently of the  $Re$ -value, the RMSEs for  $N = 4038085$  particles are always less than  $\sim 1.6\%$ . On the basis of these results, a spatial resolution resulting from  $N \geq 3000000$  particles is adopted for all subsequent simulations conducted in the present study. Working with  $N = 4038085$  particles a full run was completed after  $435698$  timesteps. This took  $3.03$  hours of real time with an Nvidia Tesla V100  $16$  GB memory computer graphics card with  $5120$  CUDA cores and a maximum clock rate of  $1.53$  GHz.

The generation of suitable inflow conditions in the pipe bend is further investigated to validate the numerical procedure. Figure 4 shows intensity maps of the streamwise velocity in four cross-stream planes, i.e., at  $\theta = 30^\circ$ ,  $60^\circ$  and  $75^\circ$  within the bend and downstream the bend at  $x = d$  (i.e., at  $432$  mm from the pipe outlet for  $Re = 500$  (left) and  $Re = 1093$  (right)). The effects of a strong secondary flow are clearly seen, which in both cases displaces the region of maximum velocity to the outside of the

bend. These maps reproduce remarkably well the velocity contours that were measured experimentally by Enayet et al. [3] at the same pipe stations (see their Figs. 4 and 6). The maximum velocities are  $v/v_B \approx 2.0$  for  $Re = 500$  and  $\approx 1.91$  for  $Re = 1093$ , which are very close to the values quoted by Enayet et al. in their Figs. 4 and 6. As the liquid flows into the bend, the secondary flow develops gradually. For instance, at  $\theta = 30^\circ$  a thickening of the shear layer on the inside of the bend is already visible, while at  $\theta = 60^\circ$  and  $75^\circ$  the secondary flow is almost fully developed as shown by the C-shaped contours. The resulting cross-sectional velocity maps for the turbulent flow at  $Re = 43000$  are shown in Fig. 5 at five different stations, namely  $\theta = 30^\circ$ ,  $60^\circ$  and  $75^\circ$  within the bend and downstream the bend at 432 mm and 288 mm from the pipe outlet (see Fig. 2), corresponding to stations  $x = d$  and  $x = 6d$  downstream the bend, respectively. In the  $60^\circ$  plane, the flow has become distorted due to the presence of a strong secondary flow, which then grows and extends over and beyond the inner half of the section as shown by the velocity map at  $75^\circ$ . In much the same way as in Enayet et al.'s experiment, the large secondary flow extends over the entire flow area and persists at 288 mm from the pipe outlet, where the C-shape deformation is still evident. As in the laminar case, the morphology of the velocity maps is also seen to match very well the experimental velocity contours of Enayet et al.'s (see their Fig. 9).

Modern applications of Eq. (4) to model water at all temperatures use  $\gamma = 7$ . However, experimental fittings for pure and sea water data at  $20^\circ\text{C}$  yielded values of the exponent between  $\sim 5$  and  $\sim 8$  [64,65]. In order to test the level of dependence of the results on  $\gamma$ , we use the test model with  $Re = 43000$  and  $N = 4038085$  for  $5 \leq \gamma \leq 9$ . The results for the horizontal and vertical streamwise velocity profiles are shown in Fig. 6. As  $\gamma$  is varied the numerical profiles remain essentially the same. Table 2 lists their deviations from the experimental data. The largest RMSEs always occur for  $\gamma = 5$  and as the exponent is increased to  $\gamma = 9$  the errors converge asymptotically to the same value. This demonstrates that the results are independent of  $\gamma$ . The turbulent  $Re = 43000$  model was also used to test the level of mass conservation. The variation of the total fluid mass,  $M$ , with time can be calculated by direct integration of Eq. (13) over the pipe volume and then by summing over all fluid particles to yield

$$M^{n+1} = M^n + \Delta t \sum_{a=1}^N \frac{m_a}{\rho_a^{n+1/2}} \left( \sum_{b=1}^n m_b \mathbf{v}_{ab}^{n+1/2} \cdot \nabla_a^{n+1/2} W_{ab}^{n+1/2} \right), \quad (25)$$

where the summation term between parentheses is just the SPH representation of  $-\bar{\rho} \nabla \cdot \tilde{\mathbf{v}}$  in Eq. (13). Figure 7 depicts the time variation of the total fluid mass as calculated from Eq. (25) for all resolutions of Table 1. Mass conservation is very well reproduced by all models independently of the spatial resolution.



During the first 0.05 s the model exhibits at all resolutions peak deviations from the initial mass that are all within  $3.4 \times 10^{-5}$  kg. Thereafter, the total mass oscillates with deviations amplitudes which are less than about  $6.3 \times 10^{-6}$  kg. After 0.1 s the oscillations damp out and the total mass remains constant in time. The level of mass conservation is measured in terms of the relative error between the initial and final value of the total mass. At the lowest resolution ( $N = 247790$ ) the error is  $\approx 1.6 \times 10^{-3}\%$  and decays to less than  $1.2 \times 10^{-5}\%$  when the resolution is raised to  $N = 4038085$  particles. Finally, Fig. 8 shows the RMSEs between the streamwise velocity profiles and the experimental data as a function of the Mach number for the runs of Table 1, where the Mach number is calculated as the ratio of the maximum streamwise velocity over the sound speed of water at 20°C taken to be  $1481 \text{ m s}^{-1}$ . Since the maximum streamwise velocity increases with resolution (see Fig. 3), so does the Mach number. In all cases, however, the flow remains subsonic and the errors decrease almost linearly with the Mach number as the resolution increases.

## 4 Results

In any pipe system one would expect to find bends of various angles and sharpness. Therefore, here we compare the results of the SPH simulations with known experimental data for different curved pipe configurations.

### 4.1 Secondary flow induced by a 90° elbow

The characteristics of the secondary flow induced by a 90° elbow are further explored numerically by simulating the more recent experiments by Kim et al. [27]. In contrast to Enayet et al. [3], the geometry is such that upstream the bend the flow is now vertically upward as shown in Fig. 9. In this case, the pipe diameter is  $d = 50.8 \text{ mm}$ , with a  $66d \approx 3.35 \text{ m}$  long section upstream and a  $180d \approx 9.14 \text{ m}$  long section downstream interconnected by a 90° elbow with a radius of curvature  $R_c = 3d = 152.4 \text{ mm}$ . For this test case convergent solutions are obtained using a total number of 3684081 particles filling the entire pipe section. As for the experiments, the SPH simulations are carried out for three different flow conditions, corresponding to streamwise bulk velocities of  $v_B = 1.0 \text{ m s}^{-1}$  ( $Re = 50800$ ; Run 1),  $v_B = 2.0 \text{ m s}^{-1}$  ( $Re = 101600$ ; Run 2) and  $v_B = 4.0 \text{ m s}^{-1}$  ( $Re = 203200$ ; Run 3). Kim et al. [27] also performed CFD simulations of Sudo et al.'s [8] experiment using the OpenFOAM software with various turbulence models (see their Table 3). The Renormalization Group (RNG)  $k-\epsilon$  model with wall function was selected for investigating the flow on the basis that it reproduced the Sudo et al.'s experiments better than the other models. With 3684081 particles a run took 2.17 hours of real time and was completed after

276340 timesteps.

Figures 10 and 11 show details of the horizontal ( $y$ ) and vertical ( $z$ ) streamwise velocity profiles at stations  $S_2 = 3.5d$ ,  $S_3 = 10d$  and  $S_4 = 50d$  downstream the bend for Run 1 ( $v_B = 1.0 \text{ m s}^{-1}$ ;  $Re = 50800$ ). The SPH solutions (solid lines) are compared with Kim et al.'s experimental data (filled dots). As in the experiment, at  $3.5d$  from the elbow exit, the flow along the  $z$ -direction is shifted upward due to the induced swirling when passing through the bend, and then is redistributed downstream (see Fig. 11). However, as shown in Fig. 10 the profiles look much more symmetric along the horizontal cross lines at the same stations; an experimental feature that is also well reproduced by the present SPH simulations. A direct inspection of Figs. 12 and 13 of Kim et al. shows that the SPH solution follows the experimental profiles more closely than their RNG  $k-\varepsilon$  models. The RMSE deviations of the SPH profiles from the experimental data are  $\sim 1.7\%$  ( $x = 3.5d$ ),  $\sim 1.8\%$  ( $x = 10d$ ) and  $\sim 1.4\%$  ( $x = 50d$ ) along the horizontal cross line (Fig. 10) and similarly along the vertical cross line. At  $3.5d$  from the elbow, the horizontal ( $y$ ) profile is such that the streamwise velocity is a little augmented near the pipe wall due to swirling effects which tend to reduce the velocity in the central region. However, at  $10d$  from the bend, these velocity peaks has already been diffused by turbulent dissipation. The dependence of the flow downstream the elbow on the Reynolds number is depicted in Fig. 12, where the SPH simulations for Run 1, 2 and 3 are compared along the horizontal cross lines at the same pipe stations of Figs. 10 and 11. The similarity in the structure of the flows after the elbow is very well reproduced by the SPH calculations. As  $Re$  increases, the velocity at the center of the pipe and far from the elbow (at  $50d$ ) decreases very slightly. This feature is also very well reproduced by the SPH simulations. This happens because the flattening of the velocity profile increases with the Reynolds number in a fully developed turbulent pipe flow [66].

## 4.2 Turbulent flow in a U-bend of circular cross-section

SPH simulations of the turbulent flow in a U-bend pipe of circular cross-section are now compared with the laser-Doppler measurements of the longitudinal velocity components reported by Azzola et al. [6]. The geometry and dimensions of the strongly curved  $180^\circ$  pipe is shown in Fig. 13. The pipe diameter is  $d = 4.45 \text{ cm}$  and the bend mean radius of curvature is  $R_c = (r_0 + r_1)/2 = 3.375d \approx 15.019 \text{ cm}$ . The U-bend is attached to its  $\theta = 0^\circ$  inlet and  $\theta = 180^\circ$  outlet planes by two straight pipes of the same diameter and length equal to  $54.7d \approx 184.6125 \text{ cm}$ . The stations upstream ( $S_1 = 2d = 8.9 \text{ cm}$  and  $S_2 = d = 4.45 \text{ cm}$ ), within ( $\theta = 3^\circ, 45^\circ, 90^\circ, 175^\circ$  and  $177^\circ$ ) and downstream ( $S_3 = d = 4.45 \text{ cm}$ ,  $S_4 = 2d = 8.9 \text{ cm}$ ,  $S_5 = 3d = 13.35 \text{ cm}$ ,  $S_6 = 4d = 17.8 \text{ cm}$  and  $S_7 = 5d = 22.25 \text{ cm}$ ) the U bend, where the SPH profiles and cross-sectional contour maps of the streamwise velocity component are

compared with Azzola et al.'s data are marked by segment lines normal to the pipe outer wall. As for the experiments, the SPH simulations are performed for two different flow conditions, corresponding to mean bulk velocities  $v_B = 1.29 \text{ m s}^{-1}$  ( $Re = 57400$ ; Run 1) and  $v_B = 2.47 \text{ m s}^{-1}$  ( $Re = 110000$ ; Run 2). The associated Dean numbers,  $De = Re(d/R_c)^{1/2}$ , are  $De = 31300$  and  $59900$ , respectively. Good convergence is already observed for a total of  $N = 9200853$  particles filling the full pipe section. At this resolution a run took 1.29 hours of real time and needed 158960 timesteps to be completed.

Only streamwise velocity profiles for  $Re = 57400$  are depicted in Azzola et al.'s [6] paper (their Fig. 2). They argued that except for relatively small differences, the experimental profiles obtained for  $Re = 110000$  remained essentially the same as for  $Re = 57400$ . While this observation is in agreement with the findings of Kim et al. [27] for varying high  $Re$ -values in the range between 50000 and 200000, the same experimental trends are predicted by the SPH simulations. Figure 14 shows the streamwise velocity profiles for  $Re = 57400$  (solid gray lines) and  $Re = 110000$  (dashed lines) as compared with the experimental data of Azzola et al.'s for  $Re = 57400$  (empty circles) at the pipe stations marked in Fig. 13. The agreement between the SPH and Azzola et al.'s data is very good. The RMSE deviations between the SPH profiles and the experimental measurements vary from  $\sim 0.8\%$  to  $\sim 1.7\%$ . In all pipe stations, the SPH streamwise velocity profiles for  $Re = 110000$  are essentially the same as those obtained for  $Re = 57400$ , in good agreement with the experimental observations. A picture of the computed flow development in the U-bend is shown in Fig. 15, where cross-stream velocity intensity maps are depicted. The flow morphology reported by Azzola et al. in their Fig. 5 is very well reproduced by the SPH simulations at all pipe stations. In particular, at  $\theta = 90^\circ$  and  $135^\circ$  the maximum streamwise velocity is displaced off-axis, while at  $\theta = 177^\circ$  the velocity intensity is greater toward the outer wall of the bend, which is a clear effect of the reversal of the secondary flow on the mid-plane. The intensity maps at the downstream station  $S_7$  shows that the streamwise flow experiences a too slow recovery from the adverse pressure gradient that the fluid on the inside of the bend encounters at the bend exit.

### 4.3 Flow in a helically coiled pipe

It is well-known that helical geometry imposes a number of distinctive phenomena in the field flow compared to the most commonly studied case of straight pipes. Similar to the usual pipe elbows, the duct curvature produces a centripetal force on the circulating fluid, which gives rise to a cross-sectional pressure gradient toward the external bend of the pipe accompanied by an intense recirculation in the form of two counter-rotating vortices [32, 13]. Here we describe three-dimensional SPH simulations of water flow in a vertically oriented helical pipe by adopting the same parameters employed in Tang

et al.'s [33] experiments and CFD calculations. The geometry of the helically coiled pipe is shown schematically in Fig. 16, which is described by the pipe diameter  $d = 2r$ , the coil (or curvature) radius  $R_c$ , the coil pitch  $P = 2\pi b$  and the pipe length  $L = 2\pi R_c$ . For the present analysis  $d = 61.4$  mm,  $R_c = 662.5$  mm,  $P = 75$  mm and  $L = 4.163$  m, corresponding to model Pipe 1 of Tang et al. [33]. At the pipe inlet a flat axial velocity profile is specified, corresponding to a volumetric flow rate

$$Q = \frac{\dot{m}}{\rho} = \frac{\pi}{4} v_B d^2. \quad (26)$$

The initial conditions for eleven selected flow models are detailed in Table 3. Starting from the first column, Table 3 lists the flow rate, the corresponding bulk velocity, the Reynolds number and the Dean number, respectively. These values of  $Q$  are within the range of values consistent with Tang et al.'s experimental data. All runs for this test case were carried out with 3348466 initially uniformly distributed particles. A typical run in Table 2 took 0.93 hours of real time to complete 49170 timesteps.

Figure 17 shows the dependence of the pressure drop,  $\Delta p$ , on the flow rate,  $Q$ , as calculated with SPH (solid line) for the models listed in Table 3. The SPH results are compared with the Tang et al.'s experimental data (empty circles) and with Ito's [67] (dashed line) and Murakami et al.'s [68] (dottedline) correlations for single-phase, turbulent flow in curved pipes given by

$$f_c = \frac{1}{4} \left( \frac{r}{R_c} \right)^{1/2} \left\{ 0.029 + 0.304 \left[ \left( \frac{r}{R_c} \right)^2 \text{Re} \right]^{1/4} \right\}, \quad (27)$$

and

$$f_c = 0.079 \text{Re}^{-1/4} \left[ \text{Re} \left( \frac{r}{R_c} \right)^2 \right]^{1/20}, \quad (28)$$

respectively. Here  $f_c$  is the Fanning friction factor, which contributes to the pressure drop as

$$\Delta p = \frac{2L}{d} f_c \rho v^2, \quad (29)$$

where  $L$  is the pipe length. The SPH calculations show an acceptably good agreement with the experimental data. In terms of the RMSE metric, the deviation between the SPH and the experimentally obtained pressure drop is less than 1.6%. For comparison, Tang et al. reported a deviation between their simulated results and the experimental measurements of 2.9%. Moreover, the deviations between the two empirical calculations and the SPH results are lower than 2.6%, compared to the less than 5% deviations reported by Tang et al. Streamwise velocity intensity maps are shown in Fig. 18 at various cross-sectional planes along the pipe for the case when  $Q = 10 \text{ m}^3 \text{ h}^{-1}$  for  $Re = 644.01$  and  $De = 138.63$ . In this figure the sectional planes are identified by the angle  $\theta$  from  $0^\circ$  (pipe inlet) to  $360^\circ$  (pipe outlet). For the same cross-sections, the intensity maps are seen to reproduce very well the velocity contours reported by Tang et al. [33] in their Fig. 7. A maximum flow velocity is achieved approximately at  $\theta = 60^\circ$ . Unsteady flow develops along the circumference of the coiled pipe and the area of the region of maximum velocity reduces as the flow approaches the pipe outlet.

#### 4.4 Pulsatile flow in an S-shaped exhaust pipe

SPH simulations of pulsatile flow in an S-shaped exhaust pipe of an automotive engine are now carried out under the same conditions of the experiments conducted by Oki et al. [15]. Studying the flow conditions in such manifolds is important for maintaining the high performance of close-coupled catalytic converters, which are used as emission control devices in automotive engines. Such exhaust gas flows are in general complex because of their unsteadiness and highly turbulent nature [69]. For example, the conversion efficiency and durability of the converter are both increased when a uniform flow is established.

Figure 19 shows a schematic of the S-shaped exhaust pipe. The pipe has a  $32 \text{ mm} \times 32 \text{ mm}$  square section and two  $57.7^\circ$  bends with a radius of curvature  $R_c = 50 \text{ mm}$ . The instantaneous velocity which is supplied to the pipe inlet is displayed in Fig. 20 and closely follows that given by Oki et al. [15] in their Fig. 8, corresponding to two engine cycles of period 0.08 s each in the case of 1500 rpm. The pulsation period is 0.02 s, which is a quarter of the period per engine cycle. For this test, the three dimensionless parameters of importance are the Reynolds number, the Dean number and the Womersley number [70] defined as

$$\alpha = \frac{d}{2} \left( \frac{\omega}{\nu} \right)^{1/2}, \quad (30)$$

where  $\omega$  is the angular frequency of pulsation. This number is a measure of the interaction between the inertial effects due to the pulsation and the viscous effect. The calculated flow parameters are  $Re = 48000$ ,  $De = 27200$  and  $\alpha = 70.9$ . As shown in Fig. 19, streamwise velocity profiles and cross-sectional contours are obtained numerically at  $S = 25.2$  mm downstream the second bend outlet, where Oki et al.'s experimental measurements were provided. In this case, the pipe volume was filled with 3984368 particles. With this resolution the simulation took 0.97 hours of real time to complete 57404 timesteps.

Figure 21 shows streamwise velocity maps along the pipe bends. In agreement with the experimental data, the flow velocity is higher in a region around the inner wall side of the bends as a consequence of the pressure becoming lower in these regions [8]. A comparison with Oki et al.'s Fig. 9(b) and (d) shows that the SPH simulations reproduce quite well the experimental data as obtained from their two-dimensional two-component (2D2C) PIV measurements. The SPH results for the cross-sectional streamwise flow velocity after passing through the second bend at station S are shown in Fig. 22. A comparison with the experimental counterpart (see Fig. 10(a) of Oki et al.) shows that the SPH simulations are reproducing very well the details of the flow. Figure 23 compares the numerically calculated streamwise velocity profile (solid line) with the experimental data as obtained from their 2D2C PIV (empty squares) and stereoscopic (2D3C) PIV measurements (empty circles). The SPH results fit very well the experimental data with maximum RMSE deviations of 0.8% (for 2D2C PIV) and 1.2% (for 2D3C PIV). Finally, Fig. 24 displays streamwise (intensity maps) velocity fields at the (a) first bend inlet plane, (b) first bend outlet plane, (c) second bend inlet plane and (d) second bend outlet plane. As in the CFD results of Oki et al. [15] (see their Fig. 15), at the entrance of the first bend the streamwise velocity is higher toward the inner side wall of the pipe. The same is true at the exit of the first bend. As in the first bend, at the entrance of the second bend the flow velocity is higher toward the inner side wall and, due to the cross-sectional pressure gradient in the radial direction of curvature, a well-marked C-shaped profile forms which is still evident at the second bend exit.

## **5 Concluding remarks**

Experimental data, concerning the flow characteristics within curved pipes for a wide range of Reynolds numbers ( $Re$ ) and different pipe geometries, were numerically reproduced in this article with the aid of a weakly compressible Smoothed Particle Hydrodynamics (WCSPH) method coupled to new non-reflecting outflow boundary conditions. A large-eddy simulation (LES) model was employed for the SPH calculation of turbulent flow in the pipe bends. The numerical methodology was validated against

Enayet et al.'s [3] experimental data for flow in a  $90^\circ$  pipe bend for  $500 \leq Re \leq 43000$ .

A quantitative assessment of the SPH methodology was carried out by comparing the numerical results with experimental and CFD data of turbulent flow in a  $90^\circ$  pipe bend for  $50800 \leq Re \leq 203000$  [27], in a U pipe bend for  $57400 \leq Re \leq 110000$  [6], in a helically coiled pipe for  $322 \leq Re \leq 831.8$  [33] and in an S-shaped exhaust pipe of square cross-section for pulsatile flow at  $Re = 48000$  [15]. The assessment showed that the present model is able to reproduce the experimental flow data for primary streamwise and secondary swirling velocity fields along curved pipes of different geometry with sufficiently good accuracy for a wide range of  $Re$  values. Maximum root-mean-square (RMSE) deviations between the experimental and numerical streamwise velocity profiles were always found to be within  $\sim 1.8\%$ . Cross-sectional contour velocity plots upstream, along and downstream the pipe bends were also quantitatively reproduced by the SPH simulations of the various cases. In particular, the contour shapes and the swirl intensities displayed very similar characteristics to the experiments. The agreement of the flow characteristics with the experimental data shows the uprising capabilities of the present SPH scheme for handling engineering applications involving complicated swirling flows in bends and manifolds.

## Acknowledgements

C.E.A.-R. is a research fellow commissioned to the University of Guanajuato (under Project No. 368) and he thanks financial support from CONACYT under this project. The calculations of this paper were performed using computational facilities at the Barcelona Supercomputer Center and ABACUS-Laboratorio de Matemática Aplicada y Cómputo de Alto Rendimiento of Cinvestav. We acknowledge funding from the European Union's Horizon 2020 Programme under the ENERXICO Project (Grant agreement No. 828947) and under the Mexican CONACYT-SENER-Hidrocarburos (Grant agreement No. B-S-69926).

## References

- [1] Humphrey, J. A. C., Whitelaw, J. H., and Yee, G., 1981. "Turbulent flow in a square duct with strong curvature". *Journal of Fluid Mechanics*, **103**, pp. 443–463.
- [2] Taylor, A. M. K. P., Whitelaw, J. H., and Yianneskis, M., 1982. "Curved ducts with strong secondary motion: velocity measurements of developing laminar and turbulent flow". *Journal of Fluids Engineering*, **104**(3), pp. 350–359.
- [3] Enayet, M. M., Gibson, M. M., Taylor, A. M. K. P., and Yianneskis, M., 1982. "Laser-doppler

- measurements of laminar and turbulent flow in a pipe bend". *International Journal of Heat and Fluid Flow*, **3**(4), pp. 213–219.
- [4] Chang, S. M., Humphrey, J. A. C., and Modavi, A., 1983. "Turbulent flow in a strongly curved u-bend and downstream tangent of square cross-sections". *Physicochemical Hydrodynamics*, **4**(3), pp. 243–269.
- [5] Sreenivasan, K. R., and Strykowski, P. J., 1983. "Stabilization effects in flow through helically coiled pipes". *Experiments in Fluids*, **1**, pp. 31–36.
- [6] Azzola, J., Humphrey, J. A. C., Iacovides, H., and Launder, B. E., 1986. "Developing turbulent flow in a u-bend of circular cross-section: Measurements and computation". *Journal of Fluids Engineering*, **108**(2), pp. 214–221.
- [7] Fiedler, H. E., 1997. "A note on secondary flow in bends and bend combinations". *Experiments in Fluids*, **23**(3), pp. 262–264.
- [8] Sudo, K., Sumida, M., and Hibara, H., 1998. "Experimental investigation on turbulent flow in a circular-sectioned 90-degree bend". *Experiments in Fluids*, **25**(1), pp. 42–49.
- [9] Sudo, K., Sumida, M., and Hibara, H., 2000. "Experimental investigation on turbulent flow through a circular-sectioned 180° bend". *Experiments in Fluids*, **28**(1), pp. 51–57.
- [10] Sudo, K., Sumida, M., and Hibara, H., 2001. "Experimental investigation on turbulent flow through a square-sectioned 180° bend". *Experiments in Fluids*, **30**(3), pp. 246–252.
- [11] El-Gammal, M., Mazhar, H., Cotton, J. S., Shefski, C., Pietralik, J., and Ching, C. Y., 2010. "The hydrodynamics effects of single-phase flow on flow accelerated corrosion in a 90-degree elbow". *Nuclear Engineering and Design*, **240**(6), pp. 1589–1598.
- [12] Hellström, L. H. O., Sinha, A., and Smits, A. J., 2011. "Visualizing the very-large-scale motions in turbulent pipe flow". *Physics of Fluids*, **23**(1), p. 011703.
- [13] Amicis, J. D., Cammi, A., Colombo, L. P. M., Colombo, M., and Ricotti, M. E., 2014. "Experimental and numerical study of the laminar flow in helically coiled pipes". *Progress in Nuclear Energy*, **76**, pp. 206–215.
- [14] Mazhar, H., Ewing, D., Cotton, J. S., and Ching, C. Y., 2016. "Measurement of the flow field characteristics in single and dual s-shape 90° bends using matched refractive index piv". *Experimental Thermal and Fluid Science*, **79**, pp. 65–73.
- [15] Oki, J., Ikeguchi, M., Ogata, Y., Nishida, K., Yamamoto, R., Nakamura, K., Yanagida, H., and Yokohata, H., 2017. "Experimental and numerical investigation of a pulsatile flow field in an s-shaped exhaust pipe of an automotive engine". *Journal of Fluid Science and Technology*, **12**(2),



p. JFST0014.

- [16] Kalpakli, A., and Örlü, R., 2013. "Turbulent pipe flow downstream a 90° pipe bend with and without superimposed swirl". *International Journal of Heat and Fluid Flow*, **41**, pp. 103–111.
- [17] Vester, A. K., Sattarzadeh, S. S., and Örlü, R., 2016. "Combined hot-wire and piv measurements of a swirling turbulent flow at the exit of a 90° pipe bend". *Journal of Visualization*, **19**(2), pp. 261–273.
- [18] Cioncolini, A., and Santini, L., 2006. "An experimental investigation regarding the laminar to turbulent flow transition in helically coiled pipes". *Experimental Thermal and Fluid Science*, **30**(4), pp. 367–380.
- [19] Hayamizu, Y., Yamamoto, K., and Yanase, S., 2008. "Experimental study of the flow in helical circular pipes: Torsion effect on the flow velocity and turbulence". *Journal of Thermal Science*, **17**(3), pp. 193–198.
- [20] Gupta, R., Wanchoo, R. K., and Ali, T. R. M. J., 2011. "Laminar flow in helical coils: A parameter study". *Industrial & Engineering Chemistry Research*, **50**(2), pp. 1150–1157.
- [21] Pimenta, T. A., and Campos, J. B. L. M., 2012. "Friction losses of newtonian and non-newtonian fluids flowing in laminar regime in a helical coil". *Experimental Thermal and Fluid Science*, **36**, pp. 194–204.
- [22] Dean, W. R., 1927. "Xvi. note on the motion of fluid in a curved pipe". *The London, Edinburgh, and Dublin Philosophical Magazine and Journal of Science*, **4**(20), pp. 208–223.
- [23] Homicz, G. F., 2004. Computational fluid dynamic simulations of pipe elbow flow. SAND Report 3467, Sandia National Laboratories.
- [24] Tanaka, M., Ohshima, H., and Monji, H., 2009. "Numerical investigation of flow structure in pipe flow with large eddy simulation approach". In Proceedings of the ASME 2009: Pressure Vessels and Piping Division Conference, no. 77598, American Society of Mechanical Engineers, ASME, pp. 449–458.
- [25] Hüttl, T. J., and Friedrich, R., 2001. "Direct numerical simulation of turbulent flows in curved and helically coiled pipes". *Computers & Fluids*, **30**(5), pp. 591–605.
- [26] Noorani, A., Khoury, G. K. E., and Schlatter, P., 2013. "Evolution of turbulence characteristics from straight to curved pipes". *International Journal of Heat and Fluid Flow*, **41**, pp. 16–26.
- [27] Kim, J., Yadav, M., and Kim, S., 2014. "Characteristics of secondary flow induced by 90-degree elbow in turbulent pipe flow". *Engineering Applications of Computational Fluid Mechanics*, **8**(2), pp. 229–239.
- [28] Röhrig, R., Jakirlić, S., and Tropea, C., 2015. "Comparative computational study of turbulent flow

in a 90° pipe elbow.”. *International Journal of Heat and Fluid Flow*, **55**, pp. 120–131.

- [29] Dutta, P., Saha, S. K., Nandi, N., and Pal, N., 2016. “Numerical study on flow separation in 90° pipe bend under high reynolds number by  $k$ - $\epsilon$  modelling”. *Engineering Science and Technology, an International Journal*, **19**(2), pp. 904–910.
- [30] Wang, S., Ren, C., Sun, Y., Yang, X., and Tu, J., 2016. “A study of the instantaneous turbulent flow field in a 90-degree elbow pipe with circular section”. *Science and Technology of Nuclear Installations*, **2016**, p. 5265748.
- [31] DiPiazza, I., and Ciofalo, M., 2010. “Numerical prediction of turbulent flow and heat transfer in helically coiled pipes.”. *International Journal of Thermal Sciences*, **49**(4), pp. 653–663.
- [32] Jayakumar, J. S., Mahajani, S. M., Mandal, J. C., Iyer, K. N., and Vijayan, P. K., 2010. “Cfd analysis of single-phase flows inside helically coiled pipes.”. *Computers & Chemical Engineering*, **34**(4), pp. 430–446.
- [33] Tang, L., Tang, Y., and Parameswaran, S., 2016. “A numerical study of flow characteristics in a helical pipe”. *Advances in Mechanical Engineering*, **8**(7), pp. 1–8.
- [34] Glenn, A. L., Bulusu, K. V., Shu, F., and Plesniak, M. W., 2012. “Secondary flow structures under stent-induced perturbations for cardiovascular flow in a curve artery model”. *International Journal of Heat and Fluid Flow*, **35**, pp. 76–83.
- [35] van Wyk, S., Wittberg, L. P., Bulusu, K. V., Fuchs, L., and Plesniak, M. W., 2015. “Non-newtonian perspectives on pulsatile blood-analog flows in a 180° curved artery model”. *Physics of Fluids*, **27**, p. 071901.
- [36] Vester, A. K., Örlü, R., and Alfredsson, P. H., 2016. “Turbulent flows in curved pipes: recent advances in experiments and simulations”. *Applied Mechanics Reviews*, **68**(5), p. 050802.
- [37] Morris, J. P., Fox, P. J., and Zhu, Y., 1997. “Modeling low reynolds number incompressible flows using sph”. *Journal of Computational Physics*, **136**(1), pp. 214–226.
- [38] Sigalotti, L. D. G., Klapp, J., Sira, E., Meleán, Y., and Hasmy, A., 2003. “Sph simulations of time-dependent poiseuille flow at low reynolds numbers”. *Journal of Computational Physics*, **191**(2), pp. 622–638.
- [39] Basa, M., Quinlan, N., and Lastiwka, M., 2009. “Robustness and accuracy of sph formulations for viscous flow”. *International Journal for Numerical Methods in Fluids*, **60**(10), pp. 1127–1148.
- [40] Adami, S., Hu, X. Y., and Adams, N. A., 2012. “A generalized wall boundary condition for smoothed particle hydrodynamics”. *Journal of Computational Physics*, **231**(10), pp. 7057–7075.
- [41] Ferrand, M., Laurence, D., Rogers, B., Violeau, D., and Kassiotis, C., 2013. “Unified semi-analytical

- wall boundary conditions for inviscid, laminar or turbulent flows in the meshless sph method". *International Journal for Numerical Methods in Fluids*, **71**(4), pp. 446–472.
- [42] Meister, M., Burger, G., and Rauch, W., 2014. "On the reynolds number sensitivity of smoothed particle hydrodynamics". *Journal of Hydraulic Research*, **52**(6), pp. 824–835.
- [43] Federico, I., Marrone, S., Colagrossi, A., Aristodemo, F., and Antuono, M., 2012. "Simulating 2d open-channel flows through an sph model". *European Journal of Mechanics-B / Fluids*, **34**, pp. 35–46.
- [44] Liang, C., Huang, J., and Shi, W., 2014. "A new treatment for boundary of laminar flow inlet or outlet in sph". *Journal of Software Engineering*, **8**(4), pp. 321–327.
- [45] Shi, Y., Wei, J., Li, S., Song, P., and Zhang, B., 2019. "A meshless wcsph boundary treatment for open-channel flow over small-scale rough bed". *Mathematical Problems in Engineering*, **2019**, p. 1573049.
- [46] Hou, Q., Kruisbrink, A. C. H., Pearce, F. R., Tijsseling, A. S., and Yue, T., 2014. "Smoothed particle hydrodynamics simulations of flow separation at bends". *Computers & Fluids*, **90**, pp. 138–146.
- [47] Alvarado-Rodríguez, C. E., Klapp, J., Sigalotti, L. D. G., Domínguez, J. M., and de la Cruz Sánchez, E., 2017. "Nonreflecting outlet boundary conditions for incompressible flows using sph". *Computers & Fluids*, **159**, pp. 177–188.
- [48] K, R., Malinowski, L., and Sarna, P., 2011. "Measurement of flow rate in square-sectioned duct bend". *Journal of Theoretical and Applied Mechanics*, **49**, pp. 301–311.
- [49] Rosić, N. M., Kolarević, M. B., Savić, L. M., Dordević, D. M., and Kapor, S., 2017. "Numerical modelling of supercritical flow in circular conduit bends using sph method". *Journal of Hydrodynamics, Ser. B*, **29**, pp. 344–352.
- [50] Becker, M., and Teschner, M., 2007. "Weakly compressible sph for free surface flows". In Proceedings of the 2007 ACM SIGGRAPH/Europhysics Symposium on Computer Animation, ACM SIGGRAPH/Europhysics, ACM Press, San Diego, pp. 209–217.
- [51] Antuono, M., Colagrossi, A., Marrone, S., and Molteni, D., 2010. "Free-surface flows solved by means of sph schemes with numerical diffusive terms". *Computer Physics Communications*, **181**, pp. 532–549.
- [52] Yoshizawa, A., 1986. "Statistical theory for compressible turbulent shear flows, with the application to subgrid modeling". *Physics of Fluids*, **29**(7), pp. 2152–2164.
- [53] Gómez-Gesteira, M., Rogers, B. D., Crespo, A. J. C., Dalrymple, R. A., Narayanaswamy, M., and Domínguez, J. M., 2012. "Sphysics – development of a free-surface fluid solver – part 1: Theory

- and formulations”. *Computers & Geosciences*, **48**, pp. 289–299.
- [54] Monaghan, J. J., 1992. “Smoothed particle hydrodynamics”. *Annual Review of Astronomy and Astrophysics*, **30**, pp. 543–574.
- [55] Liu, M. B., and Liu, G. R., 2010. “Smoothed particle hydrodynamics (sph): An overview and recent developments”. *Archives of Computational Methods in Engineering*, **17**(1), pp. 25–76.
- [56] Colagrossi, A., and Landrini, M., 2003. “Numerical simulation of interfacial flows by smoothed particle hydrodynamics”. *Journal of Computational Physics*, **191**(2), pp. 448–475.
- [57] Lo, E. Y. M., and Shao, S., 2002. “Simulation of near-shore solitary wave mechanics by an incompressible sph method”. *Applied Ocean Research*, **24**(5), pp. 275–286.
- [58] Hernquist, L., and Katz, N., 1989. “Treesph: A unification of sph with the hierarchical tree method”. *The Astrophysical Journal Supplement Series*, **70**, pp. 419–446.
- [59] Vacondio, R., Rogers, B. D., Stansby, P. K., Mignosa, P., and Feldman, J., 2013. “Variable resolution for sph: A dynamic particle coalescing and splitting scheme”. *Computer Methods in Applied Mechanics and Engineering*, **256**, pp. 132–148.
- [60] Wendland, H., 1995. “Piecewise polynomial, positive definite and compactly supported radial functions of minimal degree”. *Advances in Computational Mathematics*, **4**(1), pp. 389–396.
- [61] Dehnen, W., and Aly, H., 2012. “Improving convergence in smoothed particle hydrodynamics simulations without pairing instability”. *Monthly Notices of the Royal Astronomical Society*, **425**(2), pp. 1068–1082.
- [62] Crespo, A. J. C., Gómez-Gesteira, M., and Dalrymple, R. A., 2007. “Boundary conditions generated by dynamic particles in sph methods”. *Computers, Materials and Continua*, **5**, pp. 173–184.
- [63] Crespo, A. J. C., Domínguez, J. M., Rogers, B. D., Gómez-Gesteira, M., Longshaw, S., Canelas, R., Vacondio, R., Barreiro, A., and García-Feal, O., 2015. “Dualsphysics: Open-source parallel cfd solver based on smoothed particle hydrodynamics (sph)”. *Computer Physics Communications*, **187**, pp. 204–216.
- [64] MacDonald, J. R., 1966. “Some simple isothermal equations of state”. *Reviews of Modern Physics*, **38**, pp. 669–679.
- [65] Li, Y.-H., 1967. “Equation of state of water and sea water”. *Journal of Geophysical Research*, **72**, pp. 2665–2678.
- [66] Zagarola, M. V., and Smits, A. J., 1997. “Scaling of the mean velocity profile for turbulent pipe flow”. *Physical Review Letters*, **78**, pp. 239–242.
- [67] Ito, H., 1959. “Friction factors for turbulent flow in curved pipes”. *Journal of Fluids Engineering*, **FE-20-1667**, Sigalotti

**81**(2), pp. 123–132.

- [68] Murakami, M., Mori, K., and Sano, K., 1971. “A study on the hydraulic loss of tubular coils”. *Bulletin of the Japan Society of Mechanical Engineers*, **14**(78), pp. 1296–1303.
- [69] Jeong, S.-J., 2014. “A full transient three-dimensional study on the effect of pulsating exhaust flow under real running condition on the thermal and chemical behavior of closed-coupled catalyst”. *Chemical Engineering Science*, **117**, pp. 18–30.
- [70] Womersley, J. R., 1955. “Method for the calculation of velocity, rate of flow and viscous drag in arteries when the pressure gradient is known”. *The Journal of Physiology*, **127**(3), pp. 553–563.

Table 1. Parameters and results of convergence tests

Table 2. Results of the  $\gamma$ -independence test in Eq. (4) for  $Re = 43000$  and  $N = 4038085$ .

Table 3. Initial conditions for the helically coiled pipe flows

Fig. 1. Graphical representation of the SPH approximation in two-space dimensions. The circle of radius  $kh$  defines the kernel support, which in three-space dimensions corresponds to a sphere of radius  $kh$ . Only neighbor particles,  $b$ , within the kernel support are used to approximate the field variables at particle,  $a$ .

Fig. 2.  $90^\circ$  pipe geometry and dimensions used for the simulations of Enayet et al.'s [3] experiments. The line segments normal to the pipe boundary mark the stations where the streamwise velocity profiles and cross-sectional maps are compared with the experimental data.

Fig. 3. Horizontal (left column) and vertical (right column) streamwise velocity profiles upstream the bend at 212.16 mm from the pipe inlet for  $Re = 500$  (top),  $Re = 1093$  (middle) and  $Re = 43000$  (bottom). The SPH results at different resolutions are compared with Enayet et al.'s [3] experimental data (empty circles). As the resolution is increased from  $N = 247790$  (dashed lines) to  $N = 4038085$  particles (solid lines) the numerical solutions asymptotically approach the experimental profiles.

Fig. 4. Cross-sectional streamwise velocity maps at different stations ( $\theta = 30^\circ$ ,  $60^\circ$  and  $75^\circ$ ) within the pipe bend and at  $x = d$  downstream the bend (i.e., at 432 mm from the pipe outlet) for  $Re = 500$  (right) and  $Re = 1093$  (left). The inside and outside of the pipe bend correspond to the bottom and top part of the circular maps, respectively. The color bars indicate the magnitude of the streamwise velocity in  $m\ s^{-1}$ .

Fig. 5. Cross-sectional streamwise velocity maps at different stations ( $\theta = 30^\circ$ ,  $60^\circ$  and  $75^\circ$ ) within the pipe bend and at  $x = d$  and  $x = 6d$  downstream the bend (i.e., at 432 mm and 288 mm from the pipe outlet) for  $Re = 43000$ . The inside and outside of the pipe bend correspond to the bottom and top part of the circular maps, respectively. The color bar indicates the magnitude of the streamwise velocity in  $m\ s^{-1}$ .

Fig. 6. Horizontal (top) and vertical (bottom) streamwise velocity profiles upstream the bend at 212.16 mm from the pipe inlet for  $Re = 43000$ ,  $N = 4038085$  particles and varying  $\gamma$  in Eq. (4) between 5 and 9. The numerical profiles are compared with Enayet et al.'s [3] experimental data (empty circles). The numerical profiles converge to the experimental one independently of  $\gamma$ .

Fig. 7. Time variation of the total fluid mass for  $Re = 43000$  and varying spatial resolution. The level of mass conservation improves with resolution.

Fig. 8. Deviations of the streamwise velocity profiles in terms of the root-mean-square errors (RMSEs) as a function of the Mach number for all runs of Table 1.

Fig. 9.  $90^\circ$  pipe geometry and dimensions used for the simulations of Kim et al.'s [27] experiments. The line segments normal to the pipe boundary mark the stations where the streamwise velocity profiles are compared with the experimental data.

Fig. 10. Horizontal (along the  $y$ -direction) streamwise velocity profiles for Run 1 with  $Re = 50800$  at stations  $S_2 = 3.5d$ ,  $S_3 = 10d$  and  $S_4 = 50d$  downstream the bend exit plane as shown in Fig. 9. The SPH profiles (solid lines) are compared with Kim et al.'s [27] experimental profiles (filled dots).

Fig. 11. Vertical (along the  $z$ -direction) streamwise velocity profiles for Run 1 with  $Re = 50800$  at stations  $S_2 = 3.5d$ ,  $S_3 = 10d$  and  $S_4 = 50d$  downstream the bend exit plane as shown in Fig. 9. The SPH profiles (solid lines) are compared with Kim et al.'s [27] experimental profiles (filled dots).

Fig. 12. Dependence of the horizontal (along the  $y$ -direction) streamwise velocity profiles on the Reynolds number. The SPH profiles for  $Re = 50800$  (solid lines)  $Re = 101600$  (empty circles) and  $Re = 203200$  (filled squares) are compared at pipe stations  $S_2 = 3.5d$ ,  $S_3 = 10d$  and  $S_4 = 50d$  downstream the bend exit plane as shown in Fig. 9.

Fig. 13.  $180^\circ$  pipe geometry and dimensions used for the simulations of Azzola et al.'s [6] experiments. The line segments normal to the pipe boundary mark the stations where the streamwise velocity profiles are compared with the experimental data.

Fig. 14. Streamwise velocity profiles at different stations upstream, within and downstream the U-bend as marked in Fig. 13. The SPH profiles (solid gray lines) are compared with Azzola et al.'s [6] experimental profiles (empty circles) for  $Re = 57400$ . For comparison the SPH profiles for  $Re = 110000$  (dashed lines) are also displayed.

Fig. 15. Cross-sectional streamwise velocity maps at different stations ( $\theta = 3^\circ$ ,  $45^\circ$ ,  $90^\circ$ ,  $135^\circ$  and  $177^\circ$ ) within the pipe bend and at  $S_3$  ( $x = d$ ),  $S_5$  ( $x = 3d$ ) and  $S_7$  ( $x = 5d$ ) downstream the U-bend for  $Re = 57400$ . The inside and outside of the pipe bend correspond to the bottom and top part of the circular maps, respectively. The color bar indicates the magnitude of the streamwise velocity in  $m\ s^{-1}$ .

Fig. 16. Schematic drawing of the helical pipe and geometrical parameters for the simulations of Tang et al. [33] experiments.

Fig. 17. Dependence of the pressure drop,  $\Delta p$ , on the flow rate,  $Q$ , for the models listed in Table 3. The SPH results (solid line) are compared with the experimental Tang et al.'s [33] data (empty circles) and the experimental correlations derived by Ito [67] (dashed line) and Murakami et al. [68] (dotted line).

Fig. 18. Streamwise velocity maps at selected cross-sectional planes along the circumference of the helically coiled pipe for flow with  $Q = 10 \text{ m}^3 \text{ h}^{-1}$ ,  $\text{Re} = 644.01$  and  $\text{De} = 69.32$ . The color bar indicates the magnitude of the streamwise velocity in  $\text{m s}^{-1}$ .

Fig. 19. Geometry and dimensions of the S-shaped exhaust pipe used in the SPH simulations of Oki et al.'s [15] experiments.

Fig. 20. Instantaneous velocity at the inlet section of the S-shaped exhaust pipe used in the SPH simulations. Figure adapted from Oki et al. [15].

Fig. 21. Streamwise velocity map on a two-dimensional slice at the symmetry ( $z = 0$ ) plane in the first (left) and second bend (right).

Fig. 22. Cross-sectional streamwise velocity map downstream the second bend at station S as shown in Fig. 19.

Fig. 23. SPH streamwise velocity profiles (solid line) at station S in Fig. 19 as compared with Oki et al.'s [15] 2D2C PIV (empty squares) and 2D3C PIV (empty circles) experimental measurements.

Fig. 24. Cross-sectional streamwise velocity fields as obtained from the SPH simulations in: (a) the first bend inlet plane, (b) the first bend outlet plane, (c) the second bend inlet plane and (d) the second bend outlet plane. The position of the first and second bend inlet and outlet planes are indicated in Fig. 19 by the dashed lines.



$N$	Re	RMSE( $v_{x_y}/v_B$ )	RMSE( $v_{x_z}/v_B$ )
247790	500	0.076	0.084
	1093	0.095	0.088
	43000	0.081	0.081
523493	500	0.043	0.041
	1093	0.051	0.045
	43000	0.046	0.050
1080924	500	0.023	0.021
	1093	0.022	0.018
	43000	0.022	0.035
2104126	500	0.017	0.013
	1093	0.005	0.007
	43000	0.016	0.020
4038085	500	0.015	0.012
	1093	0.004	0.006
	43000	0.015	0.016

TABLE 1

$\gamma$	$\text{RMSE}(v_{xy}/v_B)$	$\text{RMSE}(v_{xz}/v_B)$
5	0.017	0.023
6	0.015	0.018
7	0.015	0.016
8	0.015	0.017
9	0.015	0.017

TABLE 2

$Q$ (m <sup>3</sup> h <sup>-1</sup> )	$v_B$ (m s <sup>-1</sup> )	Re	De
5	0.469	322.01	69.32
10	0.938	644.01	138.63
15	1.407	966.02	207.95
20	1.876	1288.02	277.27
25	2.345	1610.03	346.58
30	2.814	1932.03	415.90
35	3.283	2254.04	485.22
40	3.753	2576.04	554.53
45	4.222	2898.05	623.85
50	4.691	3220.05	693.17
60	5.629	3864.06	831.80

TABLE 3

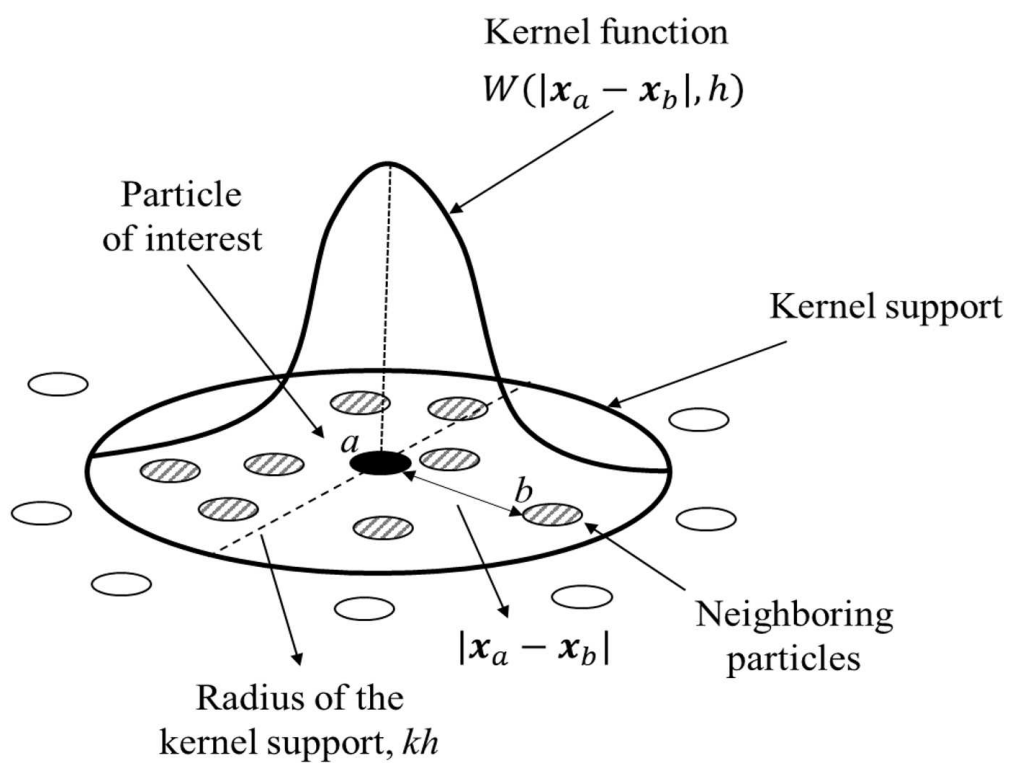


FIGURE 1

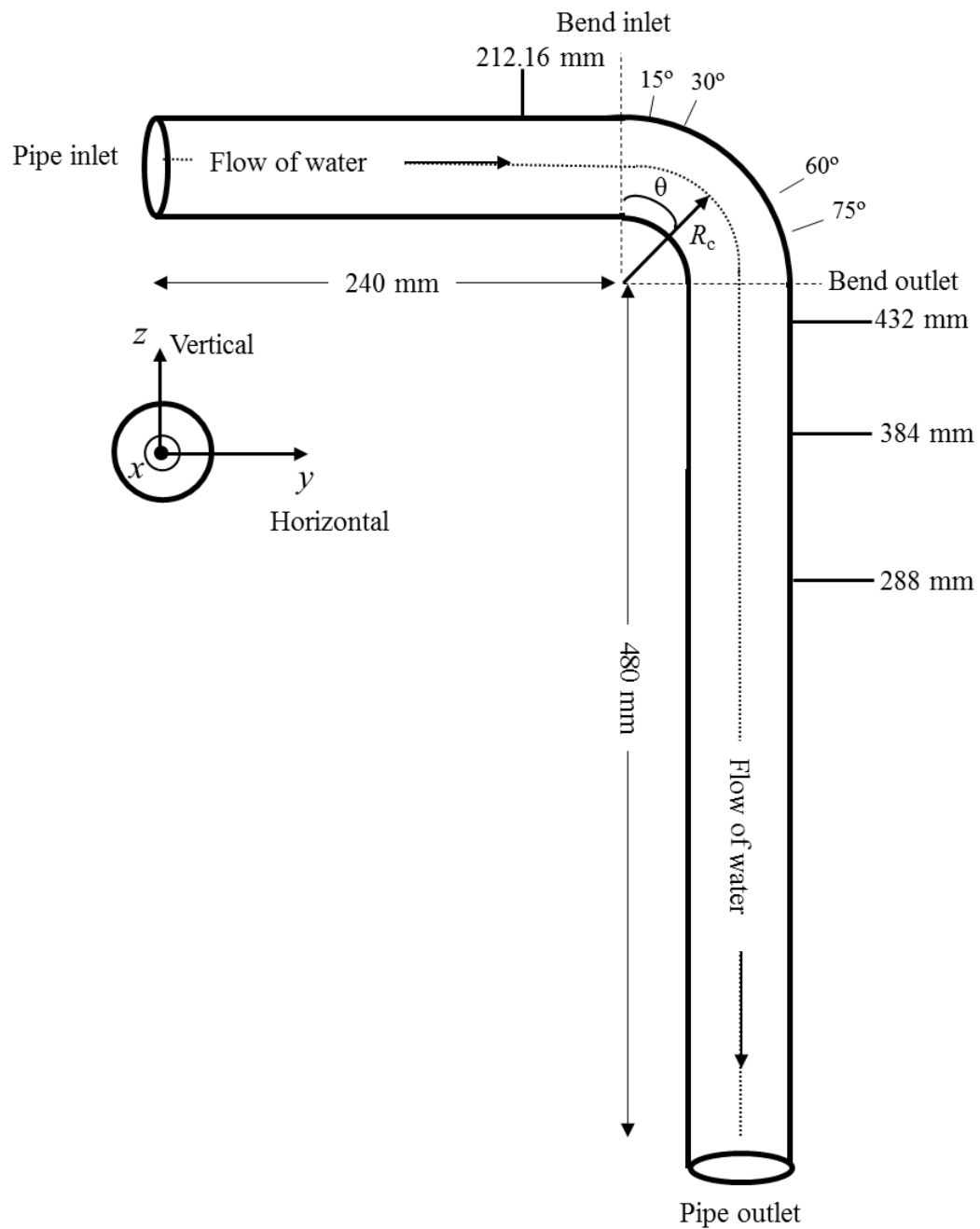


FIGURE 2

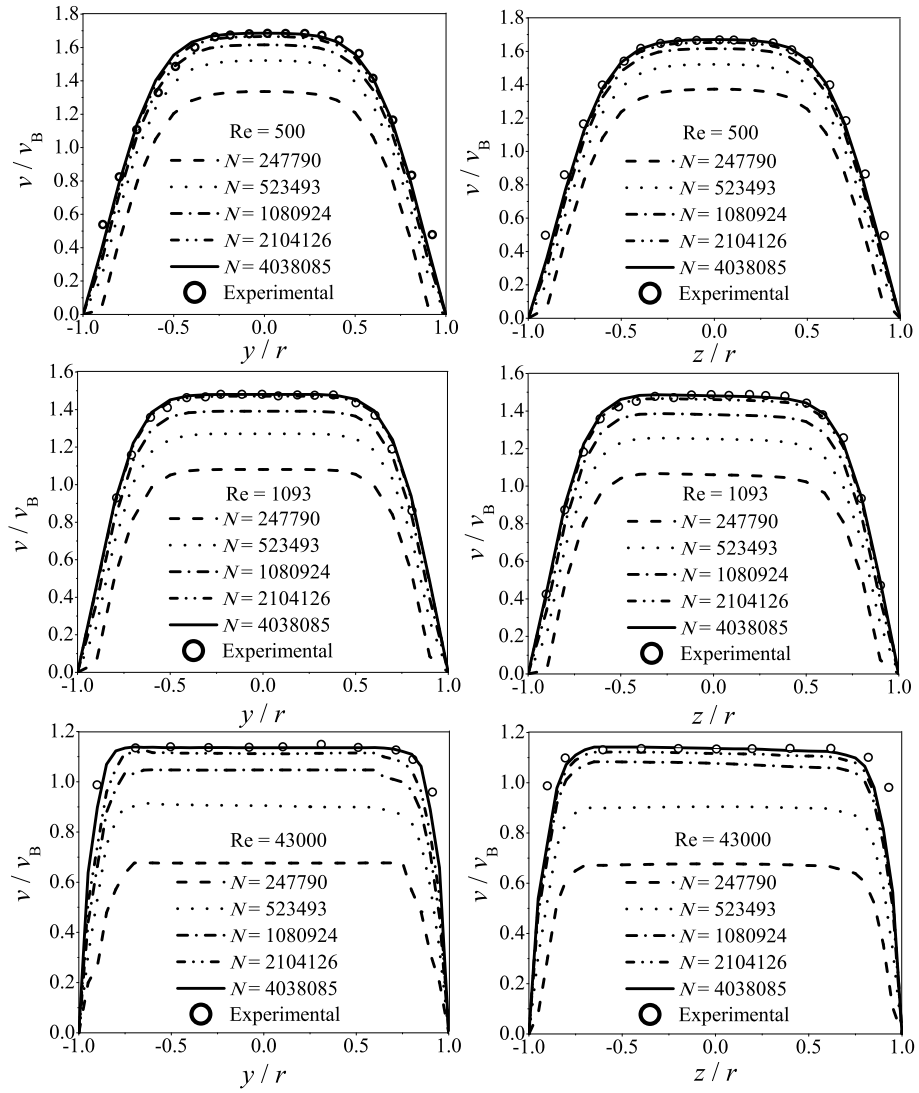


FIGURE 3

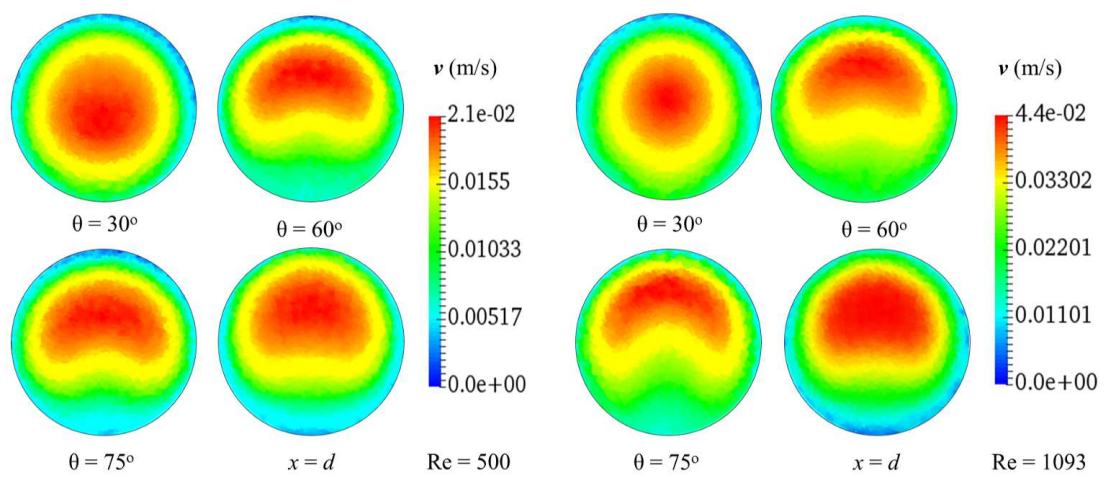


FIGURE 4

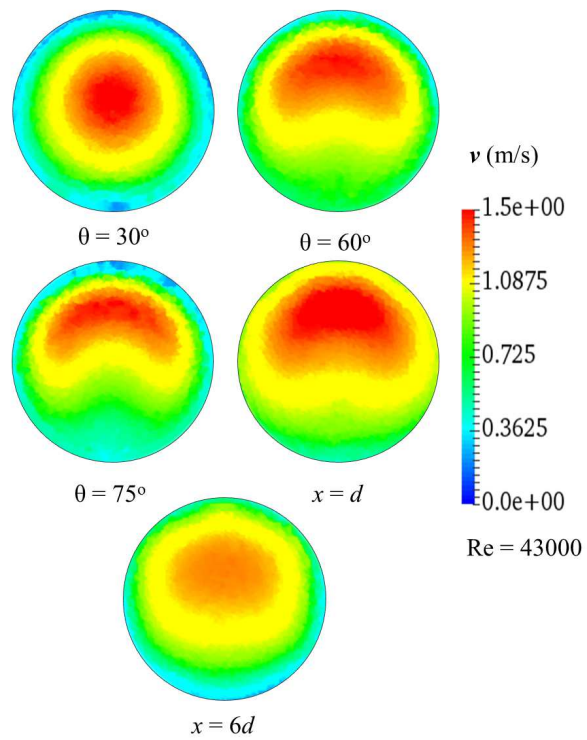


FIGURE 5



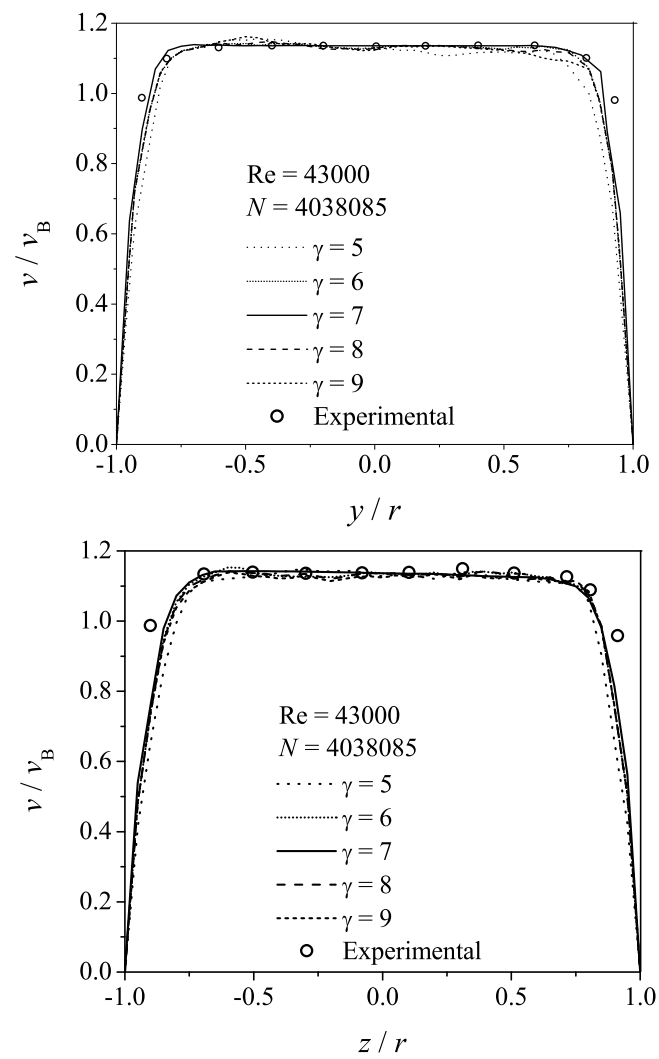


FIGURE 6

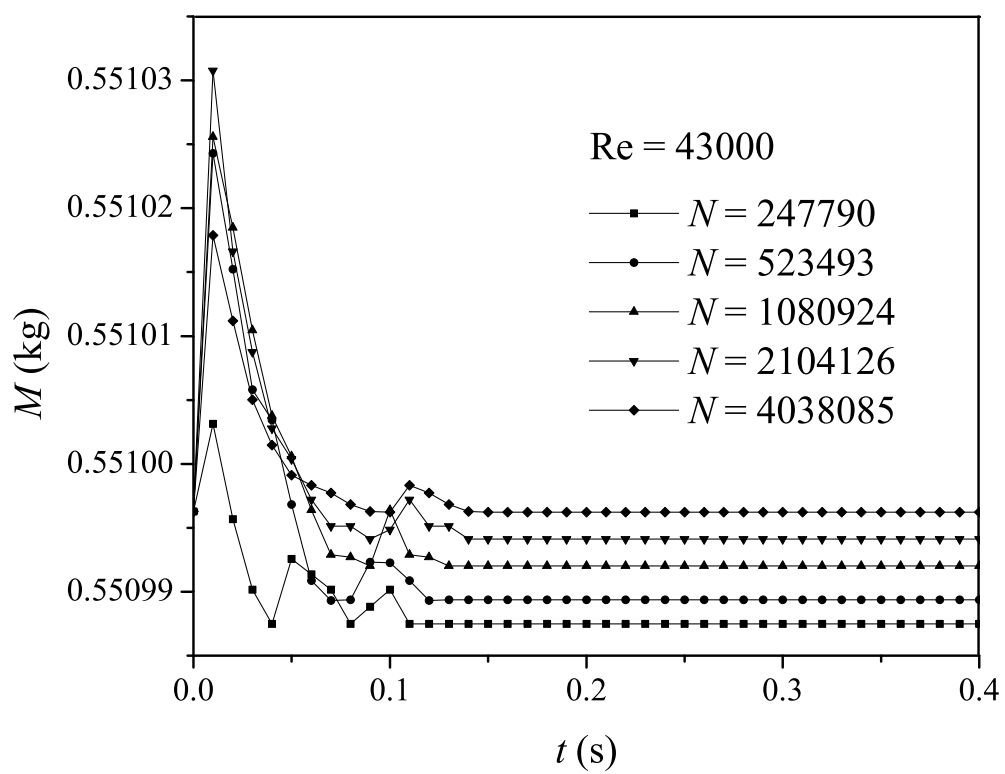


FIGURE 7

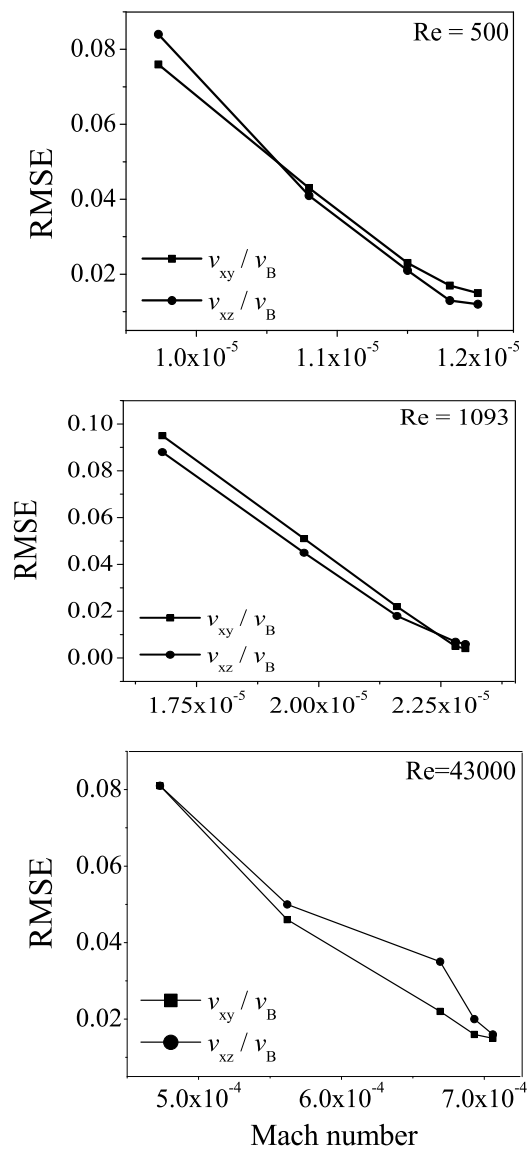


FIGURE 8

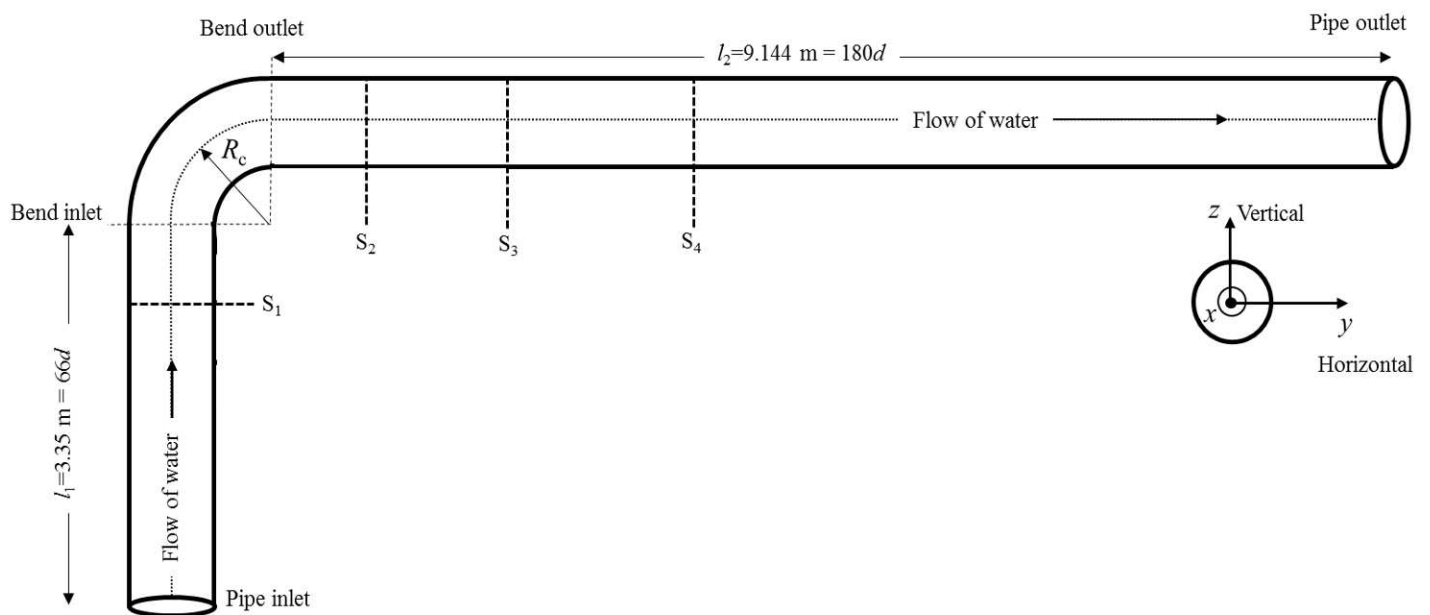


FIGURE 9

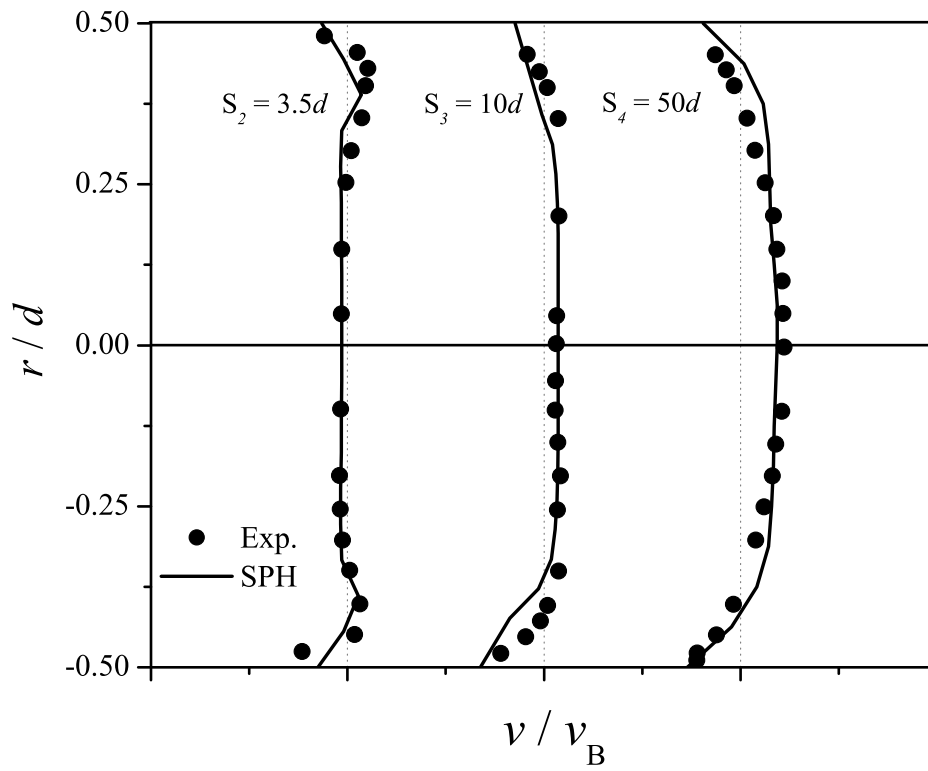


FIGURE 10

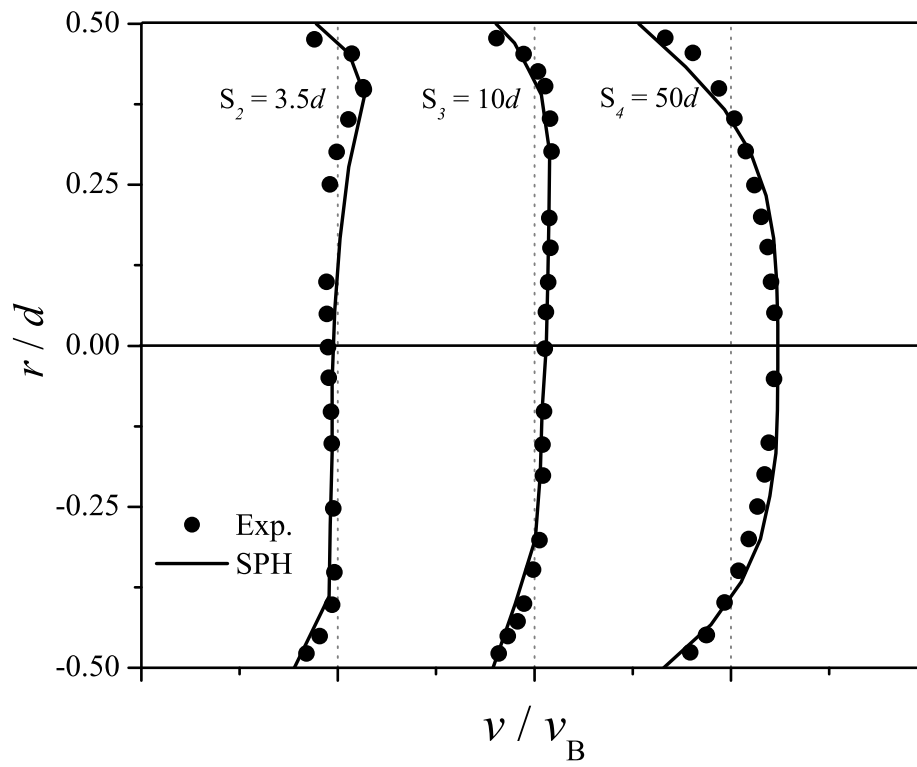


FIGURE 11

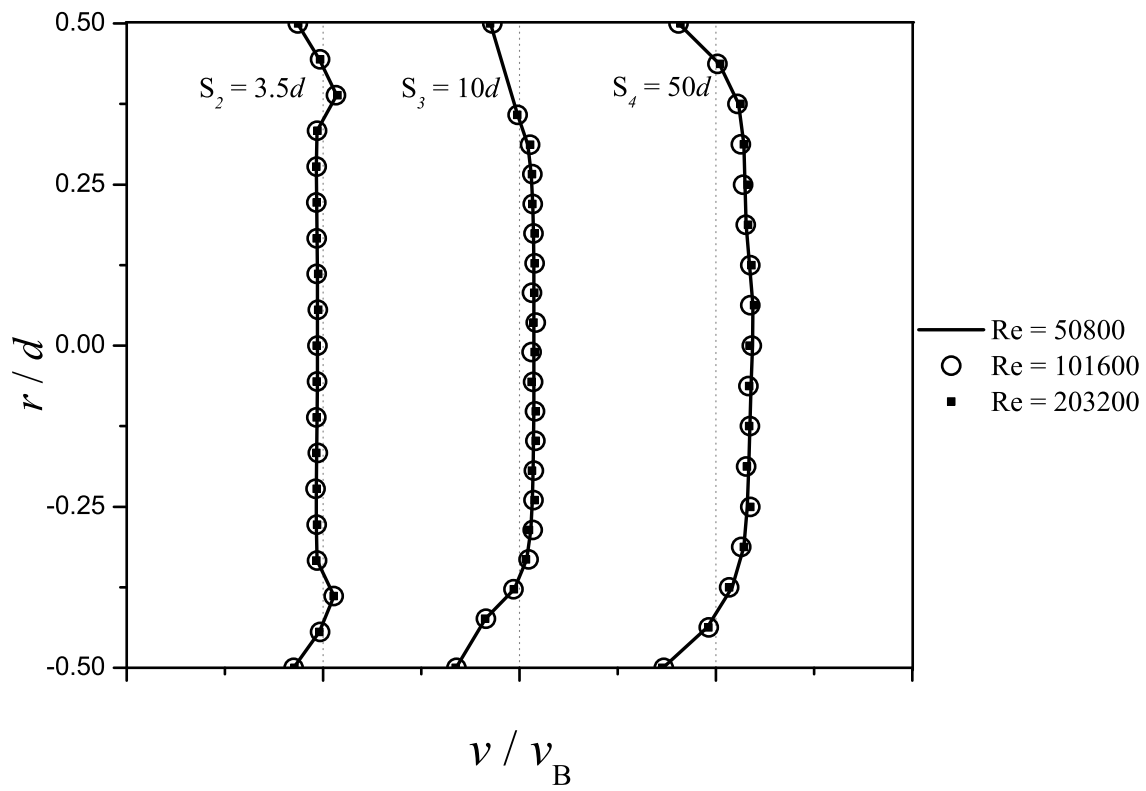


FIGURE 12

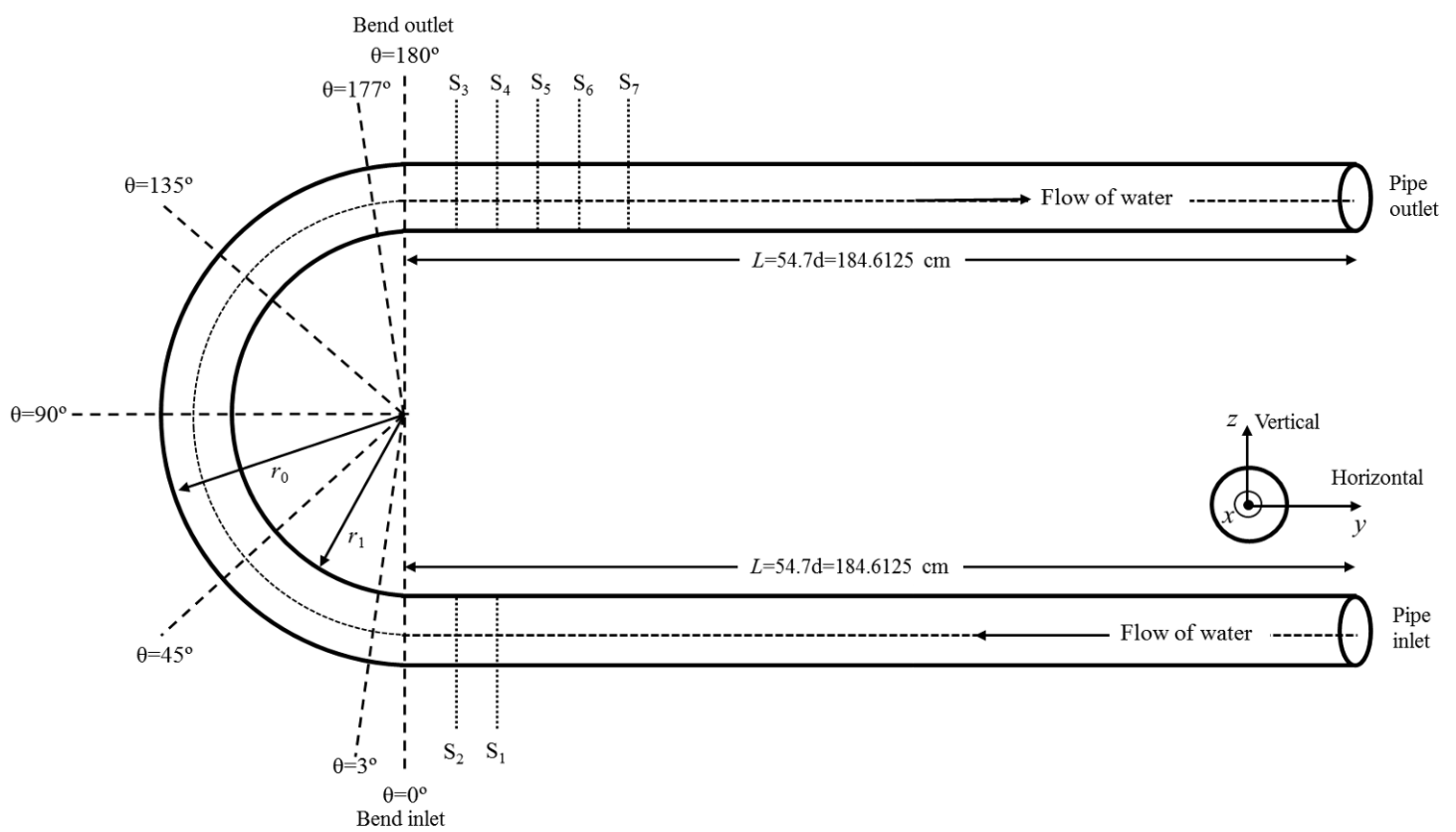


FIGURE 13



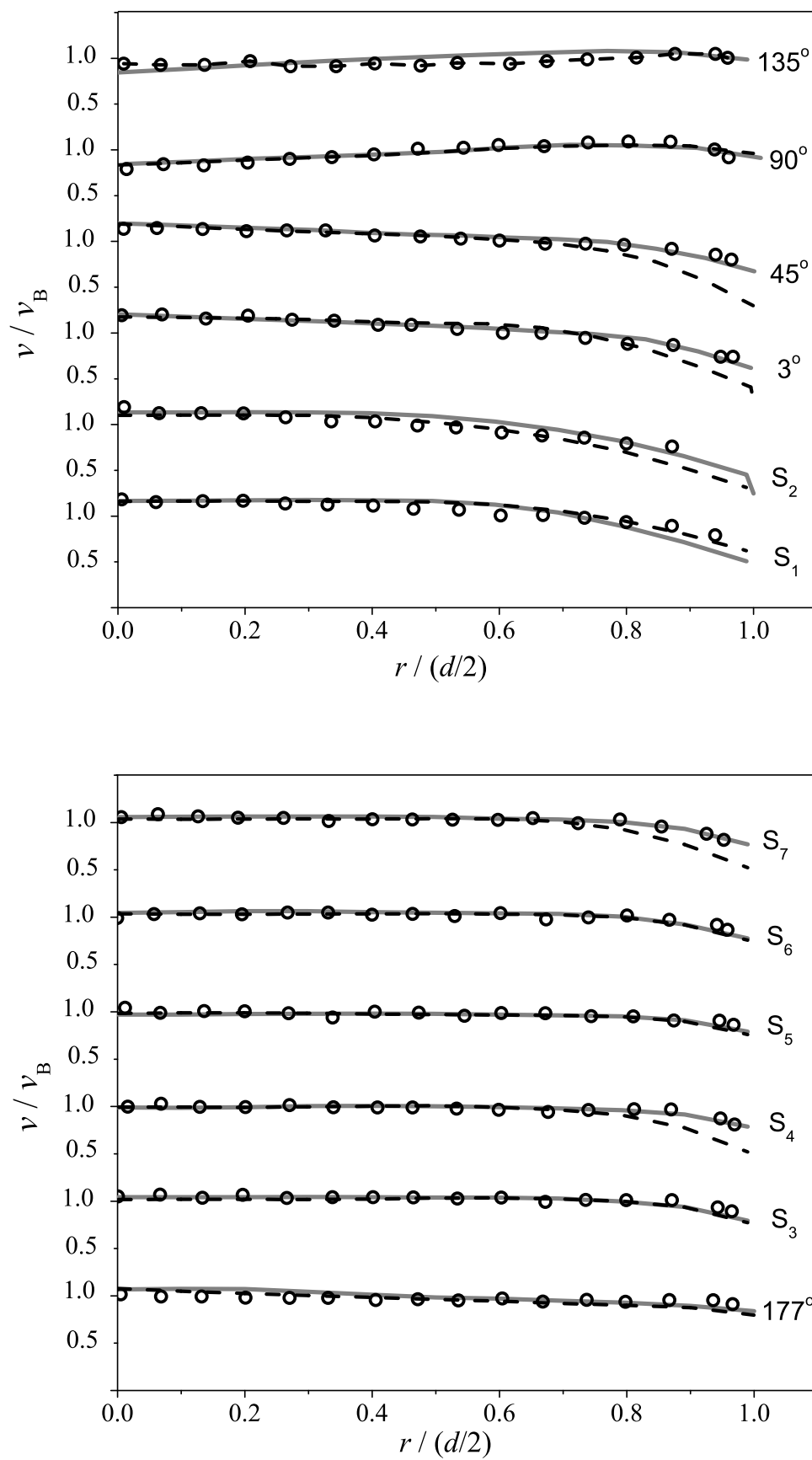


FIGURE 14

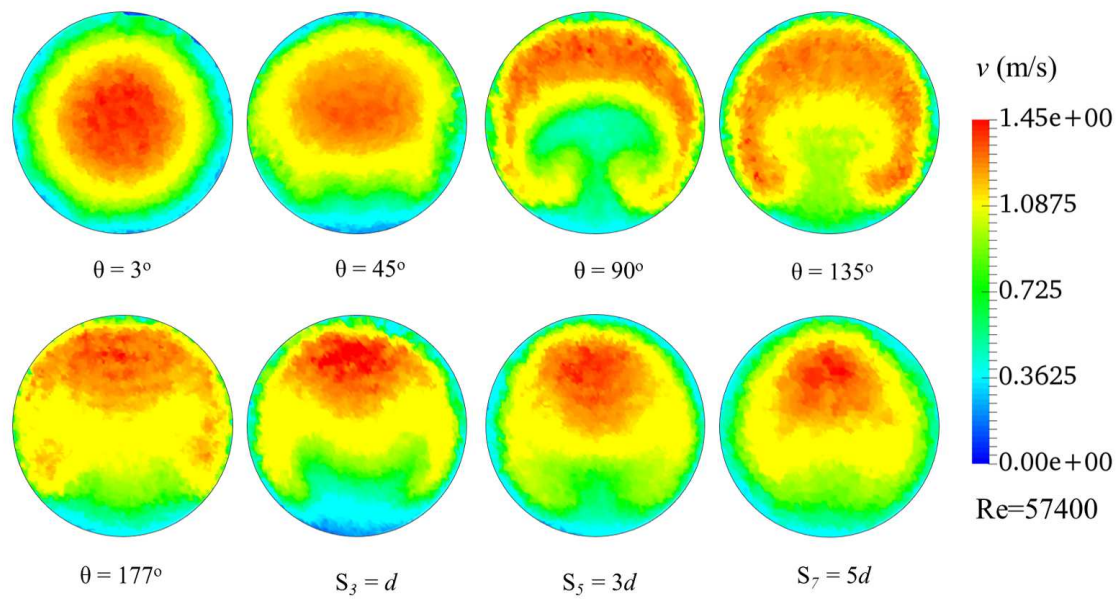


FIGURE 15

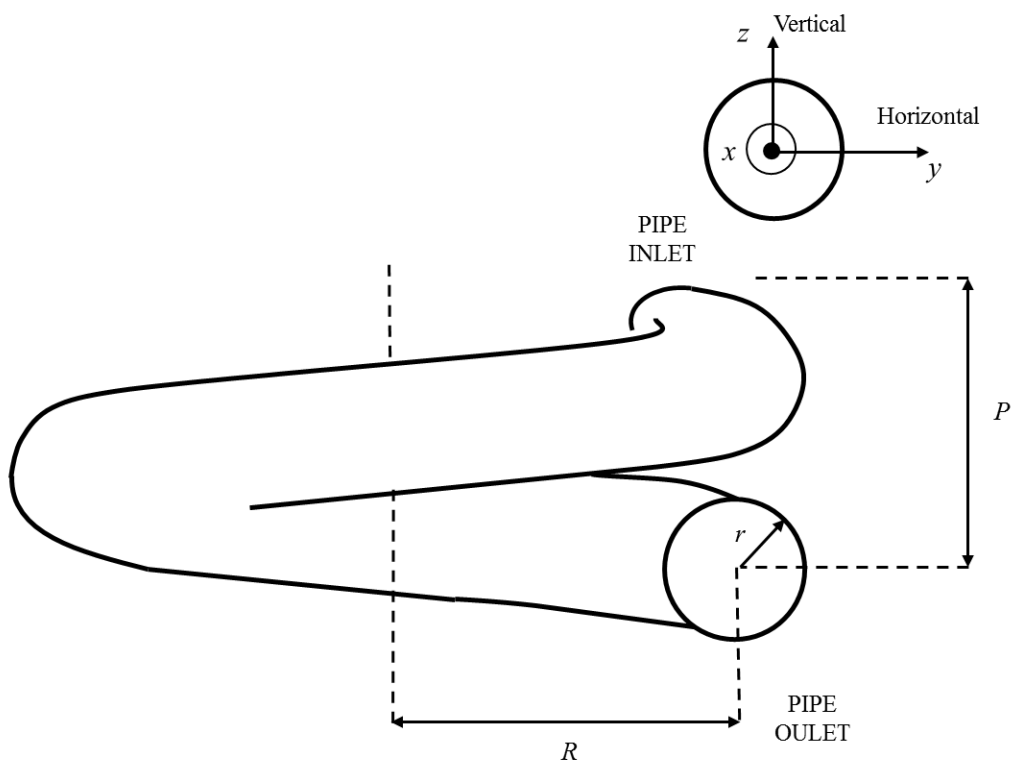


FIGURE 16

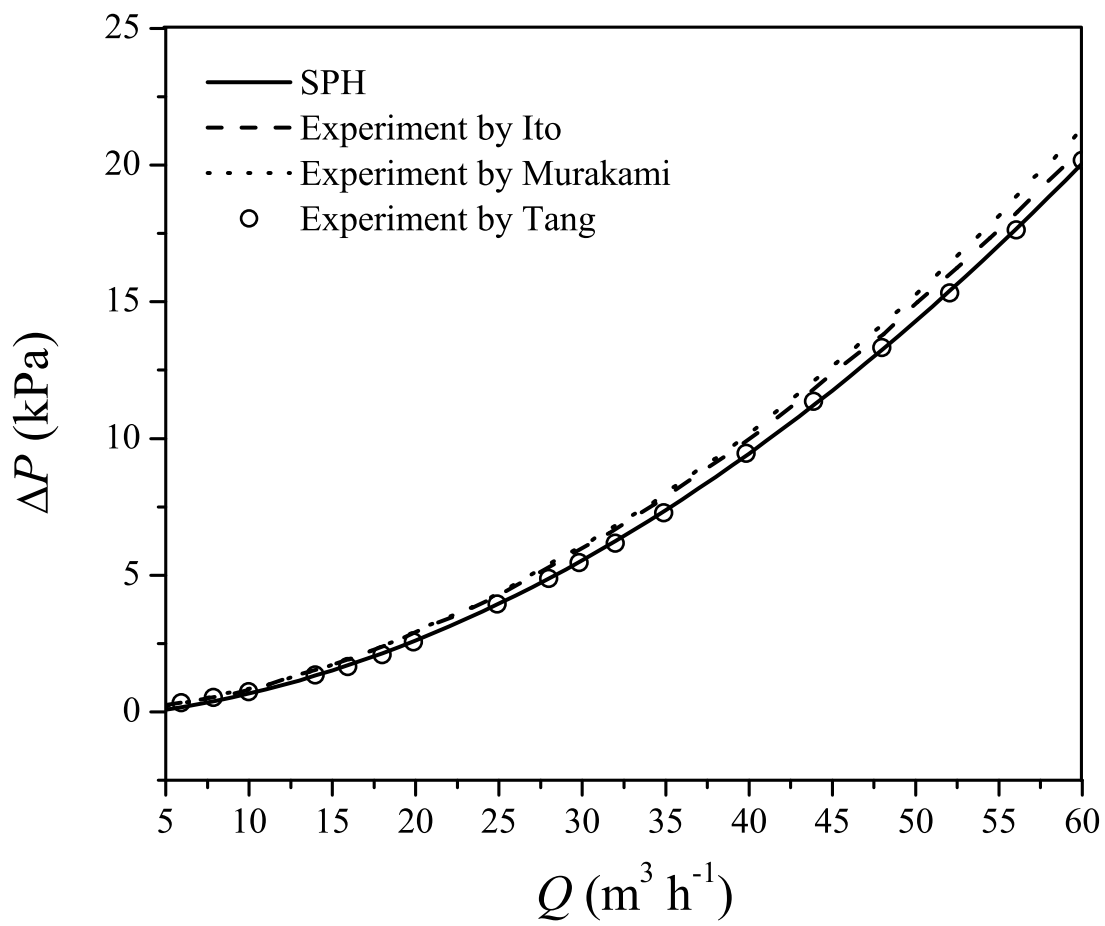


FIGURE 17

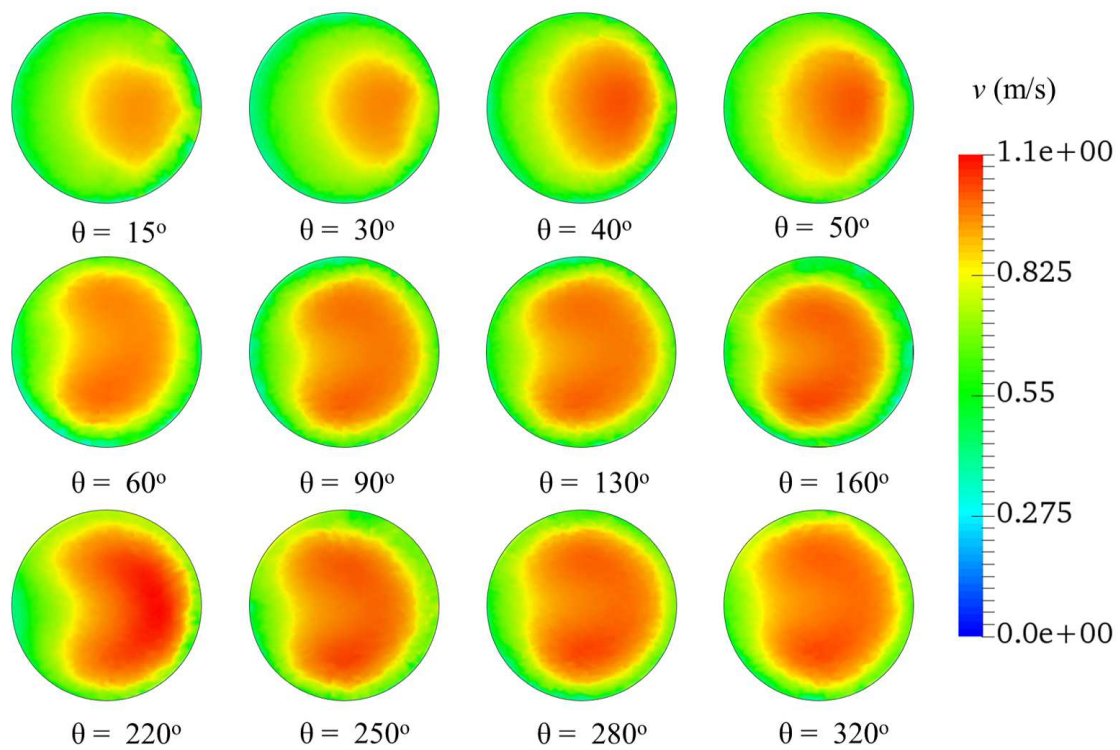


FIGURE 18

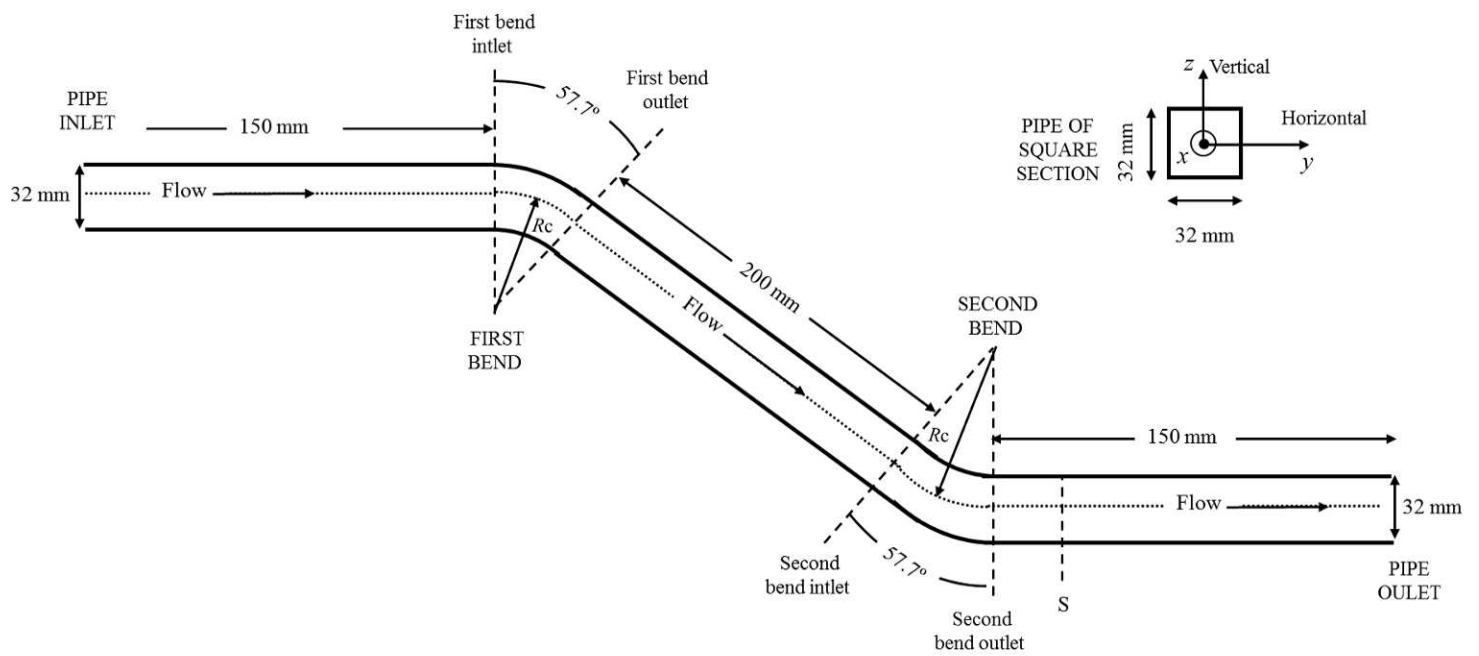


FIGURE 19

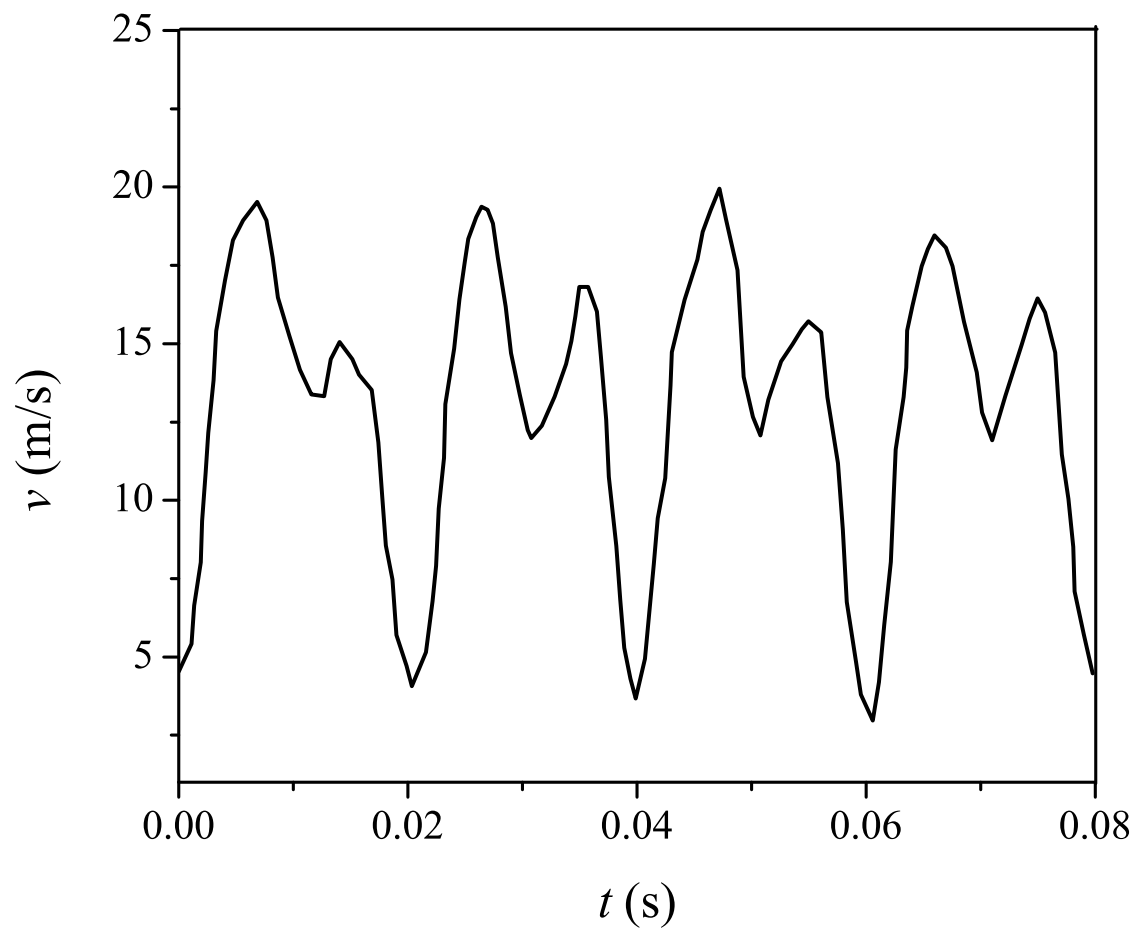


FIGURE 20

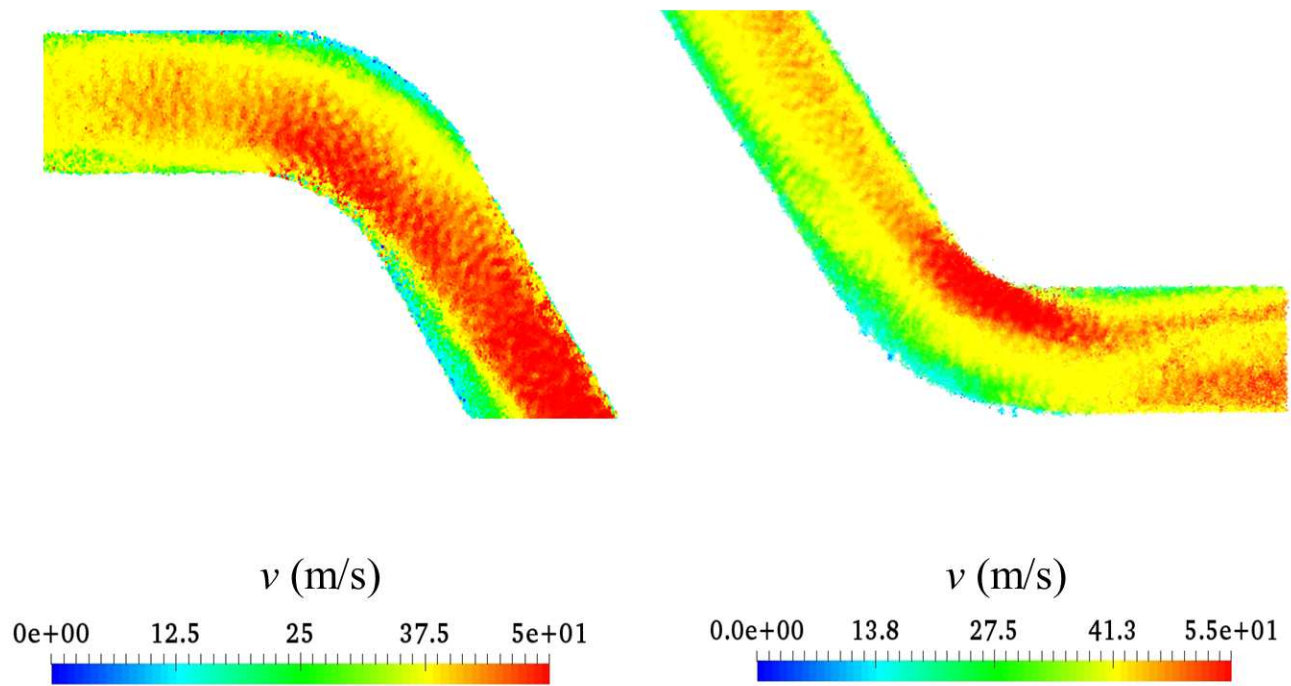


FIGURE 21



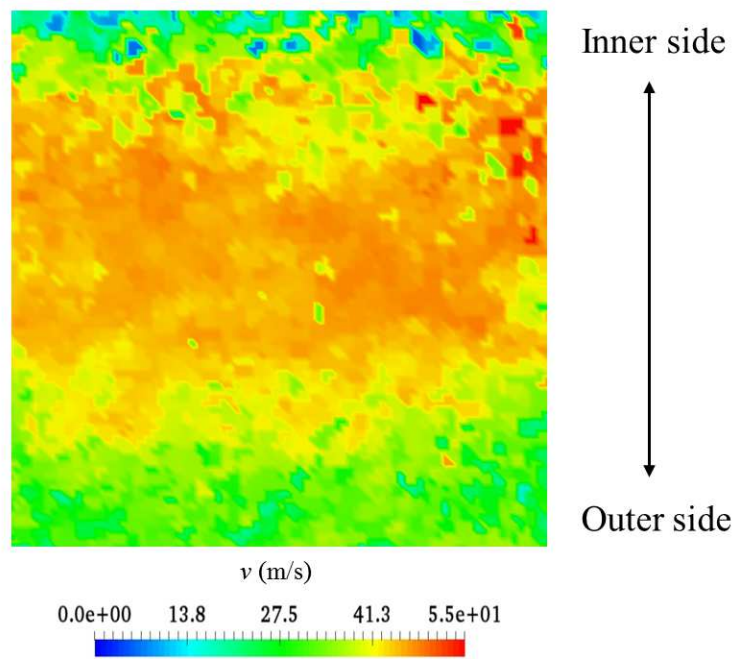


FIGURE 22

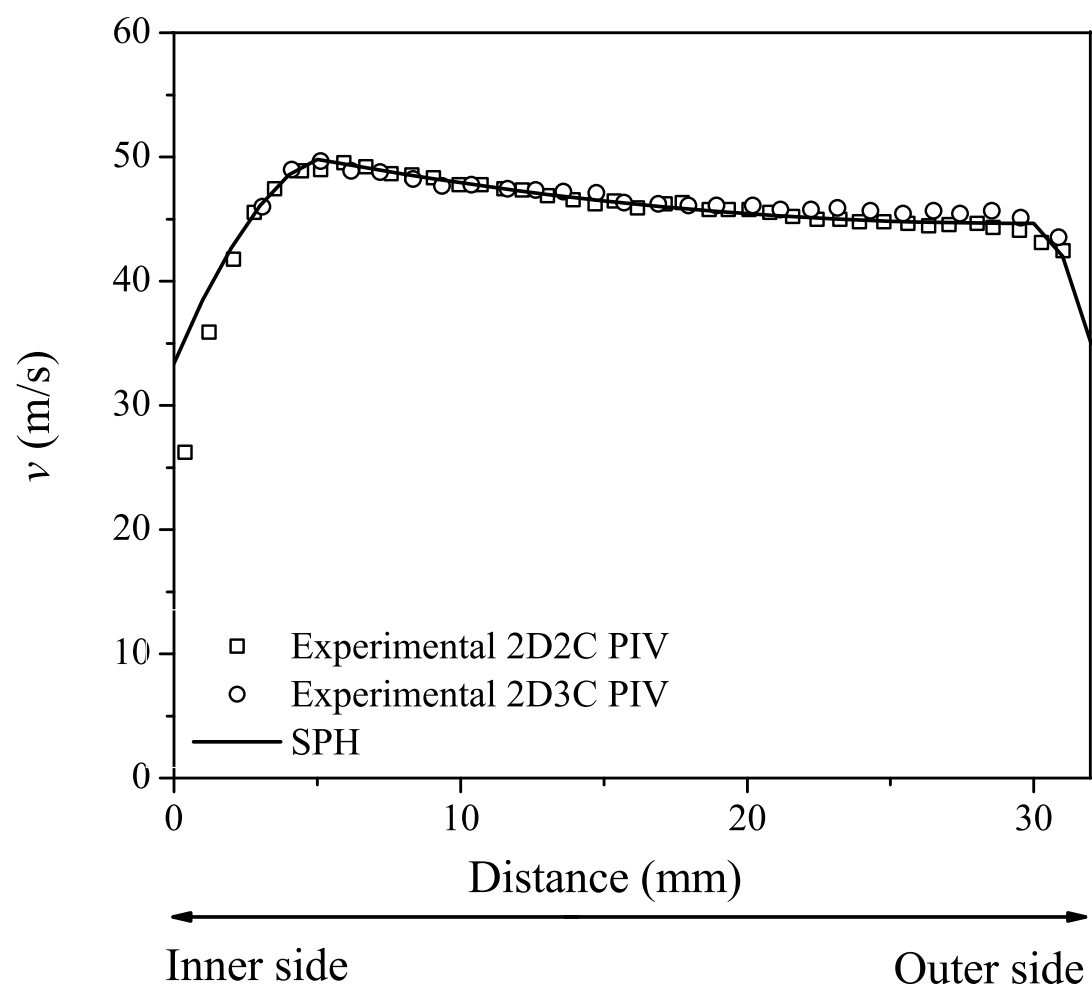


FIGURE 23

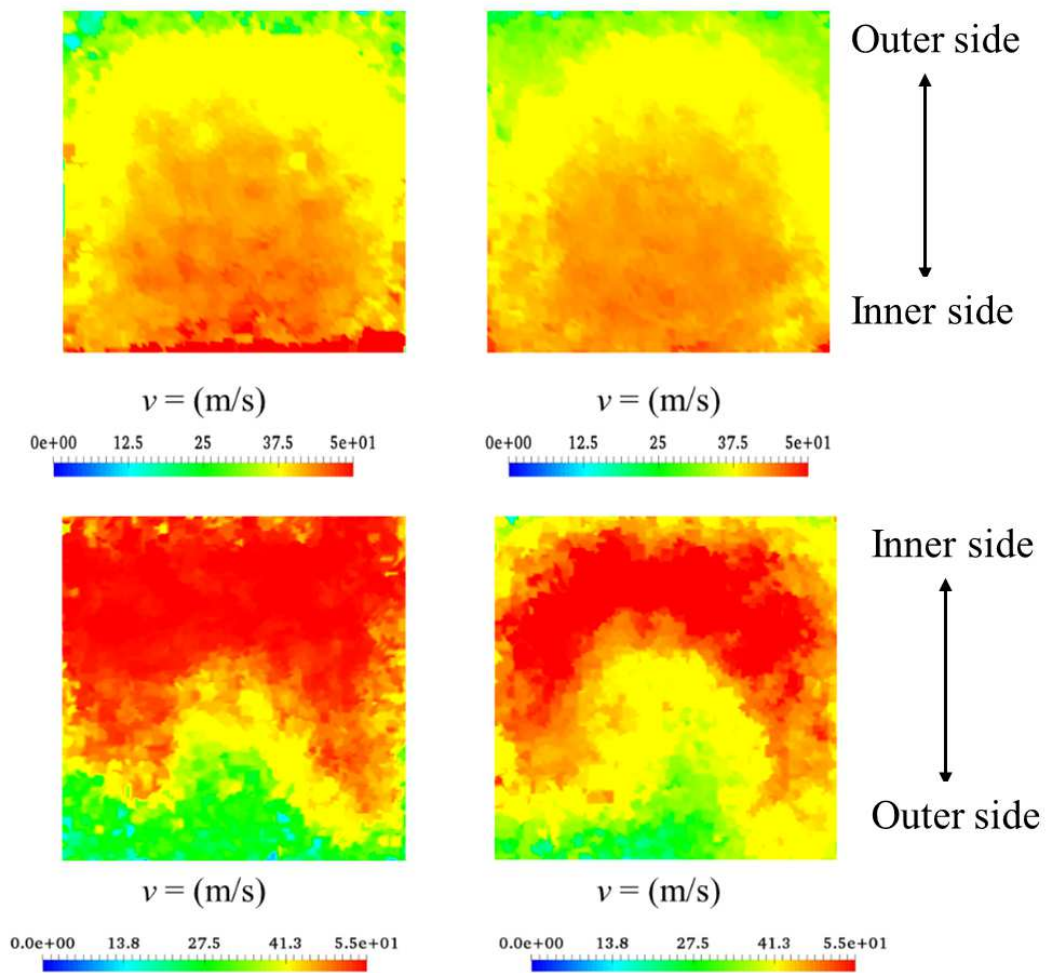


FIGURE 24

